Water mass transformation and the North Atlantic Current in three multi-century climate model simulations

Helene R. Langehaug[1,2]*, Peter B. Rhines*[3]*, Tor Eldevik*[2,4]*, Juliette Mignot*[5]*, and Katja Lohmann*[6]

[1]*Nansen Environmental and Remote Sensing Center, Bergen, Norway.*
[2]*Bjerknes Centre for Climate Research, Bergen, Norway.*
[3]*School of Oceanography, University of Washington, Seattle, Washington, USA*
[4]*Geophysical Institute, University of Bergen, Bergen, Norway*
[5]*LOCEAN, Institute Pierre Simon Laplace, University Pierre and Marie Curie, Paris, France*
[6]*Max Planck Institute for Meteorology, Hamburg, Germany*

Abstract

The warm and saline Subtropical Water carried by the North Atlantic Current undergoes substantial transformation on its way to higher latitudes as heat is released from ocean to atmosphere. The geographical distribution of the surface-forced water mass transformation is assessed in multi-century climate simulations in three different climate models, with a particular focus on the eastern subpolar North Atlantic Ocean. The models of the study are BCM, IPSLCM4, and MPI-M ESM. The diagnosis, originally introduced by Walin (1982), estimates the transformation in water mass outcrop areas from heat and freshwater fluxes. The integrated heat flux in the eastern subpolar region has a larger contribution than the freshwater flux to the water mass transformation in all three models. While the pattern of the Atlantic Meridional Overturning Ciculation (AMOC) is similar in all models, the fluxes are very different. The different pathways of the North Atlantic Current, and upper ocean low salinity water, as well as sea ice cover have strong influence on the water mass transformation. The water mass transformation in the eastern subpolar region shows pronounced variability on decadal time scale in all models, and is found to reflect the variability in the overturning circulation in two of the models with a time lag of 7-8 years.

Keywords: Water mass transformation, Subpolar Mode Water, North Atlantic Current, climate model intercomparison, decadal ocean variability.

1. Introduction

The Subtropical Water is cooled and freshened on its way northward, thereby releasing large amounts of heat to the atmosphere in the northern North Atlantic. This heat loss contributes to the relative warm European climate, both in the mean and seasonally (Rahmstorf 2002; Rhines et al. 2008). It is therefore of crucial importance to simulate the *water mass transformation* (hereafter denoted WMT) in the North Atlantic Ocean properly in climate models.

The warm and saline Subtropical Water carried by the North Atlantic Current undergoes substantial transformation in properties on its way northward from intense air-sea exchanges (Fig. 3.1; Pérez-Brunius et al. 2004; Brambilla et al. 2008). Areas of large WMT are associated with deep mixed layers and formation of Subpolar Mode Water, which is the dominant water mass above the permanent pycnocline in the northeastern North Atlantic Ocean (Fig. 3.2; McCartney and Talley, 1982; Brambilla and Talley, 2008). The Subpolar Mode Water is carried downstream from its formation region in the northeastern North Atlantic Ocean, splitting into recirculation in the western subpolar region and poleward flow into the Nordic Seas. The relative fraction of these two main branches of the North Atlantic Current is important in determining the water mass composition of the dense return flow in the North Atlantic Ocean; the Deep Western Boundary Current (Smethie and Fine 2001; Lumpkin and Speer 2003; Medhaug et al. 2011). The dense southward flow and its pathway have been very much studied (e.g., Dengler et al. 2006; Bower et al. 2009; Rhein et al. 2011).

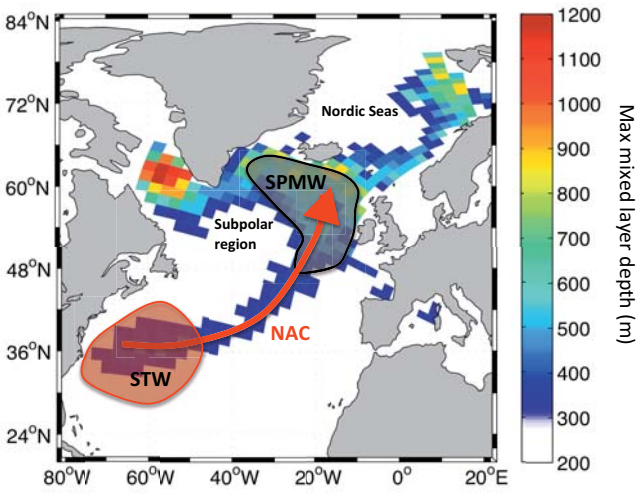

Figure 3.1: Schematics of the transformation of Subtropical Water (STW) to Subpolar Mode Water (SPMW) along the pathway of the North Atlantic Current (NAC). The mixed layer depth is deepest in March (obtained from the Bergen Climate Model).

The first objective of the present study is to investigate the magnitude and geographical distribution of the WMT in the eastern subpolar region in three different multi-century climate model simulations. The location and the typical densities of water masses involved in this WMT can be very model-dependent. Particularly the pathway of the models' North Atlantic Current defines regions of strong WMT associated with heat loss. The continuation of the North Atlantic Current into the western subpolar region and Nordic Seas, and the subsequent dense water formation and returning southward flow, have been investigated in several model studies (e.g., Mauritzen and Häkkinen 1999; Bailey et al. 2005; Medhaug et al. 2011; Langehaug et al., in revision).

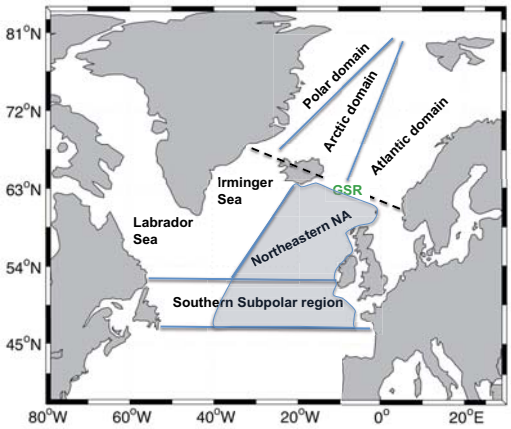

Figure 3.2: Map of the Subpolar North Atlantic (NA) and the Nordic Seas with names of geographical regions that are referred to in the text. The eastern subpolar region is indicated by the blue shaded area, and the rest as the western subpolar region. The Nordic Seas is divided into three domains after Swift (1986). The location of the Greenland-Scotland Ridge (GSR) is indicated with the dashed black line.

The North Atlantic Current forms the upper branch of the Atlantic Meridional Overturning Circulation (AMOC). The AMOC is the streamfunction of the meridional circulation in the Atlantic Ocean, with northward flow aloft and southward flow at depth (Manabe and Stouffer 1988). The variability in strength of this circulation has been investigated in a range of numerical studies, due to its climate relevance in the North Atlantic region (Bentsen et al. 2004; Jungclaus et al. 2005). The AMOC is traditionally quantified in latitude-depth space (hereafter denoted AMOCz). In the present study, where we analyze WMT, the AMOC in latitude-density space (hereafter denoted AMOCσ) is more appropriate. AMOCσ shows the density distribution associated with the overturning circulation (Mauritzen and Häkkinen 1999; Bailey et al. 2005). Particularly in the subpolar region, AMOCσ differs greatly from AMOCz, due to strong zonal density gradients (Willebrandt et al. 2001; Zhang 2010). The second objective of this study is to investigate the decadal relationship between WMT in the eastern subpolar region and AMOCσ.

In order to improve the understanding of the variability in the large-scale ocean circulation, several studies have investigated the relation between the WMT and the AMOC at high northern latitudes (Marsh 2000; Isachsen et al. 2007; Grist et al. 2009; Josey et al. 2009). Josey et al. (2009) found that the WMT due to air-sea exchanges has a significant relationship with the strength of AMOC at latitudes between 35°N and 65°N. The other source for WMT is interior mixing. Mixing plays an important role in the WMT of the Nordic Seas overflow as it descends the Greenland-Scotland Ridge and in the subsequent rising of deep water masses in the tropics (Munk and Wunsch 1998). Without interior mixing, the world ocean would gradually be filled with denser water. There are also mixing processes in the upper ocean related to the seasonal cycle of the mixed layer depth and lateral mixing of density within the mixed layer (Nurser et al. 1999).

In this study we consider the WMT due to surface forcing only; a main focus is the WMT associated with the North Atlantic Current in the upper ocean. Previous studies have shown that WMT at high northern latitudes is dominated by air-sea exchanges (Nurser et al. 1999; Tandon and Zhao 2004). Similar results were found in an observation-based study by Lumpkin and Speer (2003), who investigated WMT in the North Atlantic Ocean. However, they point out that the air-sea exchanges dominate *south* of the overflow region, i.e., south of the southern flank of the Greenland-Scotland Ridge. Pérez-Brunius et al. (2004) distinguish between the WMT of Subtropical Water in the western and eastern subpolar region, and found that water entering the Labrador Sea is mainly transformed by mixing between Subtropical Water and fresh and cold subpolar waters. In the eastern subpolar region, the focus region in this study, they found that the main factors in transforming Subtropical Water are air-sea exchanges and the entrainment of saline water from the northeastern subtropical gyre. The latter is not explicitly investigated in this study. However, the entrainment of saline water influences the surface density, and thus implicitly contribute to the WMT assessed herein.

The paper is organized as follows. The three climate models and the methods used are presented in Section 2. In Section 3, the long-term mean horizontal and vertical circulation in the North Atlantic Ocean are compared among the three different models. The models' long-term mean heat- and freshwater fluxes are compared with observation-based estimates. The geographical distribution of the WMT is estimated for each model, and compared with observation-based estimates in Section 4. The decadal variability of WMT in the eastern subpolar region is also estimated and related to the strength of AMOCσ. A summary and concluding remarks follows in Section 5.

2. Data and Method

2.1 Model descriptions

The control simulations from three different climate models are compared in the present study: the Bergen Climate Model (BCM; Furevik et al. 2003; Otterå et al. 2009), the Institute Pierre Simon Laplace Coupled Model (IPSLCM4; Marti et al. 2010; Servonnat et al. 2010), and the Max Planck Institute for Meteorology Earth System Model (MPI-M ESM; Jungclaus et al. 2010). We use multi-century simulations from the EU project THOR (Thermohaline Overturning - at Risk?), where we investigate the first 500 years after the spin-up phase of each integration. All models are run without any form of flux adjustments and are thus free to evolve following their own climates.

BCM has an atmosphere model that is run with a truncation at wave number 63 (T_L63) with 31 vertical levels. The ocean model is MICOM (Miami Isopycnic Coordinate Ocean Model; Bleck et al. 1992), and has a stack of 34 isopycnic layers in the vertical. The potential densities range from σ_2=1031.514 to σ_2=1037.800 kg m^{-3}, and a non-isopycnic surface mixed layer on top provides the linkage between the atmospheric forcing and the ocean interior. The ocean grid is almost regular with a horizontal grid spacing of approximately 2.4° x 2.4° in the North Atlantic, i.e., a resolution ranging from 150 to 200 km. The data is taken from a 700-year control integration based on pre-industrial climate and has previously been used in several climate studies (Otterå et al. 2009; Medhaug et al. 2011).

IPSLCM4 has an atmosphere model with the horizontal resolution 3.75° x 2.535° (lon x lat) and 19 vertical levels. The ocean model is OPA8 (Océan PArallélisé; Madec et al. 1997). The ocean grid has 31 vertical depth levels with 2° nominal horizontal resolution in the North Atlantic, i.e., a resolution ranging from 100 to 200 km. Note that the resolution is enhanced in the tropics and the northern North Atlantic. The data is taken from a 1000-year control integration based on pre-industrial climate and has been used in several climate studies (Servonnat et al. 2010; Gastineau and Frankignoul 2011). Note that as a result of excessive freshwater flux in the Labrador Sea, deep convection in this model only takes place in the Nordic Seas and south of Iceland (Marti et al. 2010).

MPI-M ESM has an atmosphere model that is run with T31 resolution with 19 vertical levels. The ocean model is Max Planck Institute Ocean Model (MPI-OM; Marsland et al., 2003) and has 40 vertical depth levels. The ocean grid has 40 vertical depth levels with 3° x 3° horizontal resolution. Due to the location of the grid's North Pole over Greenland, the horizontal resolution in the North Atlantic ranges from 50 to 200 km. The data is taken from a 3000-year long control integration based on pre-industrial climate (Jungclaus et al. 2010).

The freshwater fluxes for the three models are implemented in different ways: The freshwater flux (F_{flx}) for BCM is calculated from the virtual salt flux (VS_{flx}) and salinity (S) as $F_{flx} = -VS_{flx}/(SC)$, where C is the constant 1*10^{-3} g kg^{-1} to convert to the units of kg

m^{-2} s^{-1}. The virtual salt flux includes all freshwater sources: evaporation (E), precipitation (P), and contributions from river runoff (R) and sea ice melting/freezing. The freshwater flux for IPSLCM4 also includes all sources, and the free surface formulation of Roullet and Madec (2000) is applied in this model. MPI-M ESM uses a semi-implicit free surface scheme (Marsland et al. 2003). For the MPI-M ESM integration presented in this study, the surface fresh water flux output contains only the atmospheric part (i.e., P-E+R). The salt flux into the ocean due to sea ice melting and freezing is taken into account during the model integration, but cannot be diagnosed afterwards, since the freezing and melting of sea ice is implemented in the ocean component of the model (no external sea ice model is used for MPI-M ESM; personnel communication Helmuth Haak). The fresh water flux from MPI-M ESM is provided in units of m s^{-1}, and to convert this flux to the units of kg m^{-2} s^{-1} it has been multiplied by the density of fresh water (1000 kg m^{-3}).

2.2 Observation-based surface fluxes

The heat- and freshwater fluxes from the models are compared with observation-based data. We have used heat flux from the National Oceanography Centre, Southampton datasets (NOC1.1a; Grist and Josey 2003; Josey et al. 1999). This dataset is based on ship data from the period 1980 to 1993, and the ocean heat budget is closed to -5 W m^{-2} using inverse analysis. The data set is distributed as a monthly climatology. Note that the NOC1 climatology was previously referred to as the Southampton Oceanography Centre (SOC) flux climatology. The observation-based freshwater flux is obtained from NCEP atmospheric reanalysis (Kalnay et al. 1996). The NCEP reanalysis is using numerical models to perform data assimilation with past data from 1948 to the present. The annual mean freshwater flux is calculated from precipitation, evaporation, and water runoff on monthly time scale for the period 1948-2010. It is important to note that these observation-based surface fluxes can contain large uncertainties. This is particularly the case for freshwater flux from NCEP. In this study we only use the long-term annual mean of the observation-based heat- and freshwater fluxes.

2.3 Water mass transformation diagnosed from surface buoyancy fluxes

The estimation of the WMT is done following the method that was introduced by Walin (1982) and further developed by Speer and Tziperman (1992). The approach is based on the fact that surface heat and freshwater fluxes modify the temperature and salinity at the ocean's surface and thereby convert water from one density class to another - assuming the temperature and salinity changes are not density-compensated. Walin (1982) and Speer and Tziperman (1992) showed that the WMT of surface waters in an outcrop region due to air-sea exchanges is equivalent to the volume transport across the outcropping isopycnal. In this study we only consider the surface-forced WMT. This means that density changes due to cooling/heating of the ocean surface, evaporation, precipitation, and contributions from river runoff and ice melting/freezing are taken into account. Density changes due to interior mixing between different water masses

are neglected. The model data applied in this analysis are monthly mean fields, while AMOCz and AMOCσ are calculated from annual means.

The surface density flux D (kg m^{-2} s^{-1}) is the key factor in the calculation of the WMT. The density flux is computed from the buoyancy flux B (kg m^{-1} s^{-3}), which includes surface heat flux Q (W m^{-2}) and freshwater flux F_{flx} (kg m^{-2} s^{-1}) into the ocean, as well as surface salinity S (dimensionless). The density flux has one thermal (F_T) and one haline (F_S) component:

$$D = B/g = F_T + F_S \tag{3.1}$$

$$F_T = \alpha c_w^{-1} Q \tag{3.2}$$

$$F_S = -\beta S F_{flx} \tag{3.3}$$

where c_w is specific heat of water (3996 J kg^{-1} K^{-1}), g is gravitational acceleration (9.81 m s^{-2}), and α and β is the thermal expansion coefficient and haline contraction coefficient, respectively. We have here used the UNESCO formulas (McDougall 1987) to calculate α and β.

The complete water mass transformation G can be expressed as the sum of the surface-forced water mass transformation F and the derivative of the diffusive density flux D_{diff} across a given σ-isopycnal (Garrett et al. 1995; Nurser et al. 1999). The annual mean F is equal to a volume transport across the given isopycnal (i.e., diapycnal transport), and is found by integrating the surface density flux over the outcrop region for surface densities between σ and $\sigma + \Delta\sigma$ (Fig. 3.3a; Speer and Tziperman 1992):

$$G(\sigma) = F(\sigma) - \frac{\partial D_{diff}(\sigma)}{\partial \sigma} \tag{3.4}$$

$$F(\sigma) = \frac{1}{T}\int_0^T (\lim_{\Delta\sigma \to 0} \frac{1}{\Delta\sigma}\int_\sigma^{\sigma+\Delta\sigma} D dA) dt \tag{3.5}$$

where A is the area of the outcrop region and T is one year. The annual mean F is given in units of Sv (1 Sv = 10^6 m^3 s-1). In this study D_{diff} is neglected and G becomes F (Eq. 4).

In practice, to obtain geographical maps of the annual mean WMT across a given σ-isopycnal from monthly means we calculate for each grid cell the surface density flux between σ and $\sigma + \Delta\sigma$ and average over one year:

$$F_i(\sigma) = \frac{1}{N_T \Delta\sigma}\sum_{n=1}^{12} D_{n,i} dA_i, n = 1, 2, 3...12 \tag{3.6}$$

where N_T is the 12 months. Note that this F is not exact the same as the F in Equation (3.5). The F in the latter is the integrated F over the outcrop region, whereas the F in Equation (3.6) is the F in one grid cell (denoted with the index i).

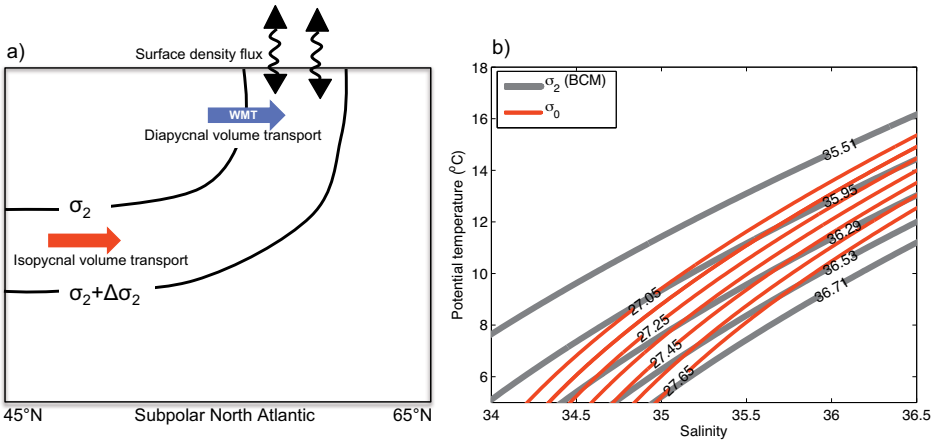

Figure 3.3: a) Schematics to describe surface-forced water mass transformation (WMT). WMT of surface water from one density class to another class due to surface density fluxes is equivalent to diapycnal volume transport (adapted from Brambilla et al. 2008). b) The typical density range of Subpolar Mode Water from observational studies is shown in red curves (in σ_0), and the density range used to capture the models' Subpolar Mode Water is illustrated by grey curves (in σ_2).

Based on previous studies the WMT from monthly data tend to overestimate the actual WMT (Tandon and Zhao 2004; Cerovecki and Marshall 2008). Eddies in the upper ocean and mixing associated with deepening of the mixed layer have been shown to contribute to the WMT with an opposite effect than the surface forcing (Tandon and Zhao 2004; Cerovecki and Marshall 2008). In this study we use climate models that are non-eddy resolving. This means that higher temporal resolution of the model data, if they were available, would not better resolve the eddy-induced bias of the WMT estimation.

Another aspect of the calculation of the WMT is the outcrop region. The summer outcrop for a given density can be located far away from the winter outcrop for the same density. For instance, cold melt water in the vicinity of the Arctic sea ice edge during summer could have similar densities as Subpolar Mode Water during winter. This means that when integrating the WMT over a year and a specific region, the water masses with the same density do not necessarily communicate with each other over a year. This will however not be an issue in the geographical distribution of the annual mean WMT.

We have used density with reference pressure of 2000 dbar (σ_2), for consistency with the vertical coordinate of the ocean model in BCM. The WMT is calculated for σ_2-densities in the

interval 34.95-36.85 kg m^{-3}. These densities correspond to the isopycnals that outcrop in the eastern subpolar region. The σ_2-densities are compared with the typical observed density range of Subpolar Mode Water in Fig. 3.3b (Brambilla and Talley 2008; Brambilla et al. 2008). $\Delta\sigma$ in Equation (3.6) is the density difference between the σ_2-densities investigated here (in kg m^{-3}), illustrated by the density difference between the grey lines in Fig. 3.3b.

To estimate the amount of new water masses that are produced due surface-forced WMT, the surface-forced formation must be calculated. The surface-forced formation is the difference in WMT across two neighboring density layers. If there is convergence, water will subduct in the densest layer of the two, i.e., accumulation of water in the densest layer, and vice versa in case of divergence, i.e., removal of water in the densest layer. Hence, this surface-forced formation expresses changes in the isopycnal transport (Fig. 3.3a). If there is no difference in the WMT across the two neighboring density layers, there is no formation of new water masses and no change in the isopycnal transport. The AMOCσ is the actual isopycnal transport derived from the models, integrated zonally and in density space. The surface-forced formation in the subpolar region is therefore compared with changes in the isopycnal transport within the subpolar region obtained from the AMOCσ in section 3.4.

2.4 Statistical methods

To filter out high-frequency variability, all time series have been low-pass filtered using an 11-year running Bartlett window. The time series are linearly detrended prior to correlation/regression analysis. For significance testing a Student's *t*-test is used together with the method of Chelton (1983) to estimate the effective number of degrees of freedom. All correlations given in the text are significant above the 95% confidence level.

3. Model climatologies in the northern North Atlantic

In this section the annual mean surface density with the barotropic streamfunction is first presented for the different models. Then sources to changes in the surface density, namely heat- and freshwater fluxes, are presented and compared with observation-based estimates. The thermal (F_T) and haline (F_S) components are calculated to compare the relative contributions of the heat- and freshwater fluxes to the surface density flux within each model. The thermal component (i.e., heat flux) dominates the haline component in the eastern subpolar region in all models. Finally, the annual mean meridional overturning streamfunction in both latitude-depth space and latitude-density space are compared among the models.

The surface density for the different models is shown in Fig. 3.4. All models have high densities in the subpolar region and in the Nordic Seas, with the densest water surfacing in the latter. The lowest densities are found in the North Sea and along the western rim of the North Atlantic, i.e., in the area of Baffin Bay, Davis Strait and Hudson Strait. These low densities

are particularly evident in IPSLCM4 and MPI-M ESM (Fig. 3.4). The annual mean barotropic streamfunction is placed on top of the surface density (contours in Fig. 3.4). The models' Subpolar Gyre and Subtropical Gyre are illustrated by their cyclonic (negative) and anti-cyclonic (positive) circulations, respectively. To emphasize the position of the North Atlantic Current, the contours at the interface between the Subpolar Gyre and the Subtropical Gyre are marked with thicker lines than the other contours. In BCM and IPSLCM4 the North Atlantic Current has a similar northeastward pathway, but the strength of the circulation is weaker in IPSLCM4 than in BCM. In MPI-M ESM the North Atlantic Current has a more zonal direction, crossing the North Atlantic Basin before flowing northward along the eastern rim of the North Atlantic Basin. There are substantial differences among the models' Subpolar Gyre shape and intensity. In all three cases, nevertheless, the North Atlantic Current crosses the North Atlantic Basin too far south compared to observational estimates (Krauss 1986; Pérez-Brunius et al. 2004).

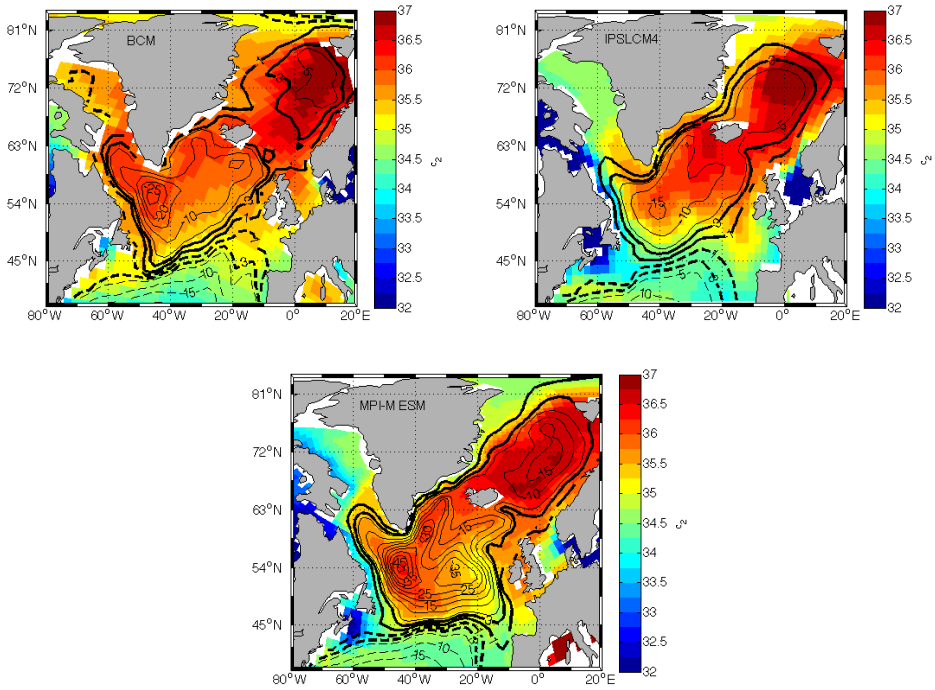

Figure 3.4: Surface density (in σ_2) for all models. Model names are indicated in the upper left corner of the figures. The barotropic streamfunction is shown in black contours (numbers are given in Sv), where negative (positive) streamfunction indicate the Subpolar (Subtropical) Gyre. Thin contours are shown with intervals of 5 Sv. Thick contours are shown for ± 1 Sv and ± 3 Sv, to emphasize the position of the North Atlantic Current at the border between the Subpolar and Subtropical gyres.

3.1 Thermal and haline contribution to the annual mean density flux

Two features dominate the comparison between the heat- and freshwater fluxes from the models and the observation-based estimates (Fig. 3.5). The first feature is the positive heat flux in NOC1.1a along the pathway of the North Atlantic Current and in the Labrador Sea. This is relatively well reproduced in BCM, except that the pathway of the North Atlantic Current is shifted eastward compared to NOC1.1a. On the contrary, in the two other models there is weak heat loss in the southern subpolar region. The reason for the weak heat loss in IPSLCM4 is that the North Atlantic Current subducts beneath the unrealistic fresh surface layer in this region (Mignot and Frankignoul 2010). In IPSLCM4 and MPI-M ESM the long-term mean heat loss is positive mainly in the vicinity of the Greenland-Scotland Ridge and in the eastern part of the Nordic Seas. The second feature is the excessive freshwater input close to Newfoundland in IPSLCM4 and MPI-M ESM compared to NCEP and BCM. The source for this excessive freshwater input points both to stronger precipitation and weaker evaporation compared to NCEP. Possible explanation for these model differences is discussed in the following comparison of the thermal and haline components, that is the heat and freshwater fluxes expressed in terms of buoyancy, and comparison of the sea ice extents.

The thermal and haline contribution to the annual mean density flux determine the magnitude of the WMT (Equation 3.1 and 3.5). We therefore compare the haline and thermal contributions to the density flux, to better understand differences in the WMT at northern high latitudes among the models (Fig. 3.6). Positive values of the thermal contribution mean that heat is lost from the ocean to the atmosphere, thereby contributing to denser surface water. Negative values of the haline contribution mean freshwater input to the ocean, as a result of net precipitation, river runoff, or sea ice melting. Overall the northward flowing water becomes denser as a result of buoyancy forcing, although changes in the haline and thermal contribution can regionally produce lighter surface water. Geographically, the haline contribution dominates or is comparable to the thermal contribution in the westernmost half of the Nordic Seas (the Polar/Arctic domain in Fig. 3.2), while the thermal contribution dominates in the eastern part of the Nordic Seas (the Atlantic domain in Fig. 3.2). In the eastern subpolar region the thermal contribution dominates the surface density flux, except in IPSLCM4 where the thermal and haline contribution are comparable (Table 3.1). In the western subpolar region the three model simulations differ: In BCM the thermal contribution dominates, in IPSLCM4 the haline contribution dominates, and in MPI-M ESM the two are of comparable size (Table 3.1).

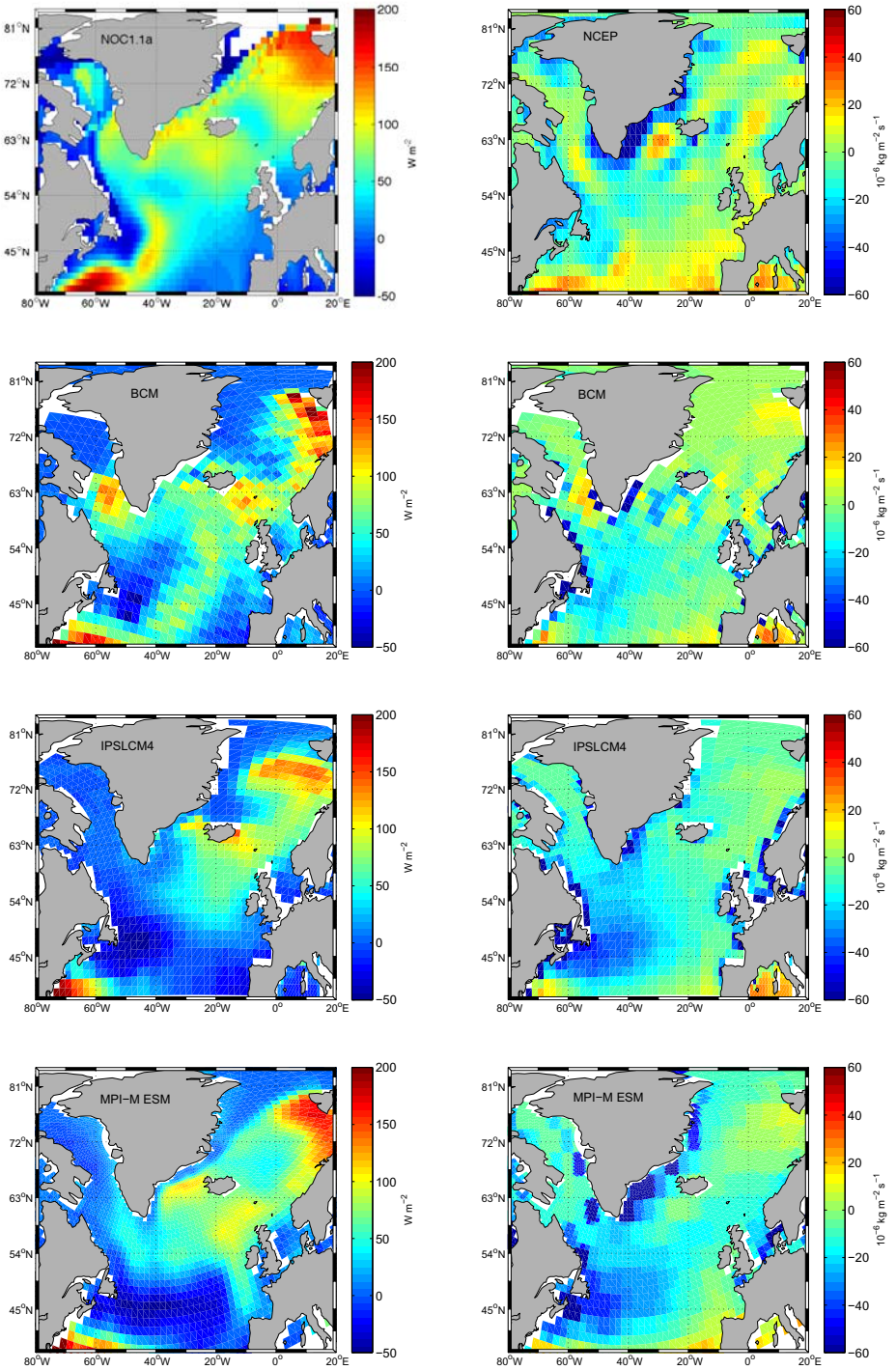

Figure 3.5: The annual mean net heat loss from ocean (left; W m^{-2}) and net freshwater loss from ocean (right; quantified as virtual salt flux, kg m^{-2} s^{-1}) from the different models and observation-based estimates (upper panel). The freshwater flux is calculated from: Precipitation - Evaporation + Runoff. Model names and source for observational based data are indicated in the upper left corner of the figures.

The haline contribution in the Nordic Seas has a similar structure in BCM and IPSLCM4, with a broad band of negative density flux in the Polar/Arctic domain. This haline contribution is located between the maximum and minimum sea ice extent in September throughout the 500 years of each simulation (Fig. 3.6), suggesting that the haline contribution is dominated by sea ice melting. Similar haline contribution in the Nordic Seas is not evident in MPI-M ESM. This is most likely related to absent contribution from ice melting/freezing in the freshwater field from MPI-M ESM. In the western subpolar region, the haline parts in both MPI-M ESM and IPSLCM4 contribute to a negative density flux covering a broad region. The maximum and minimum sea ice extent in March is illustrated in grey contours in Fig. 3.6. Both in IPSLCM4 and MPI-M ESM the sea ice extent in March can reach south of Newfoundland and eastward to about 40°W. In BCM the sea ice extent in March is only reaching the northern part of the Labrador Sea.

The excessive sea ice extent in the Labrador Sea in IPSLCM4 and MPI-M ESM, compared to observations (Johannessen et al. 2004), could be related to the pathway of the North Atlantic Current. In IPSLCM4 the barotropic circulation is generally weaker than in the other two models (Fig. 3.4), and in the western subpolar region the heat flux is weak (Fig. 3.5). The distance between the Labrador Sea and the pathway of the North Atlantic Current in MPI-M ESM is larger than in the other two models (Fig. 3.4), and the heat loss is weak in the Labrador Sea (Fig. 3.5). Both IPSLCM4 and MPI-M-ESM have been found to have a cold bias in the western subpolar region (Jungclaus et al. 2006; Marti et al. 2010). Weak advection of heat and salt into the Labrador Sea accommodates an extensive sea ice cover in this region. In addition, fresher water requires less cooling to form sea ice. The excessive sea ice extent in the Labrador Sea can also be related to the anomalous positive net precipitation close to Newfoundland in IPSLCM4 and MPI-M ESM relative to NCEP (Fig. 3.5). The weaker evaporation close to Newfoundland is most likely linked to absence of the North Atlantic Current at surface in this region.

Regarding the thermal contribution to the mean density flux, the structure and magnitude in BCM are quite different from those of the other two models. This is particularly the case in the southern subpolar region and in the Labrador Sea, where BCM has a strong positive density flux (Fig. 3.6). These model differences are related to the differing pathway of the North Atlantic Current and the excessive freshwater input close to Newfoundland in IPSLCM4 and MPI-M ESM, as discussed above. In IPSLCM4 and MPI-M ESM there are low values of the thermal contribution in the southeastern part of the subpolar region, whereas there is a negative thermal contribution close to Newfoundland, where water becomes more buoyant. The latter is the model representation of the warming of the Labrador Current in summer time. There is also a similar contribution in the BCM in the summer months (not shown), but the annual mean is nevertheless slightly positive. Generally, the thermal contribution in BCM is larger than that in IPSLCM4 and MPI-M ESM (Table 3.1). All models agree on a dominant thermal contribution in the vicinity of the Greenland-Scotland Ridge and in the northeastern Nordic Seas.

One standard deviation of interannual variability of the thermal and haline component is calculated, to give an estimate of the magnitude of temporal variations (Fig. 3.6). The thermal contribution has largest variability along the pathway of the models' North Atlantic Current. In BCM there is also large variability in the Labrador Sea, while variability is low in this region in the other two models. In BCM the thermal variability in the Atlantic domain of the Nordic Seas (Fig. 3.2) is of similar magnitude to the variable heat loss associated with the North Atlantic Current. This is also the case for MPI-M ESM in the northern Atlantic domain. In BCM and IPSLCM4 the haline contribution has largest variability in the Irminger Sea/Denmark Strait and the Polar/Arctic domain of the Nordic Seas. The haline contribution has low variability in MPI-M ESM.

Table 3.1

Mean thermal (F_T) and haline (F_S) contribution (in 10^{-6} kg m^{-2} s^{-1}) to the surface density flux in the Nordic Seas (63-79°N, 40°W-20°E) and the eastern (E) and western (W) subpolar region (47-63°N, 60°W-10°E). The eastern and western region is separated at 35°W. Note that ice melting/freezing is not taken into account in the F_S for MPI-M ESM.

	BCM		**IPSLCM4**		**MPI-M ESM**	
Region	F_T	F_S	F_T	F_S	F_T	F_S
E subpolar	2.72	-0.35	1.25	-0.47	2.22	-0.41
W subpolar	1.18	-0.55	-0.02	-1.00	0.72	-0.77
Nordic Seas	2.20	-0.59	1.13	-1.07	1.50	-0.86

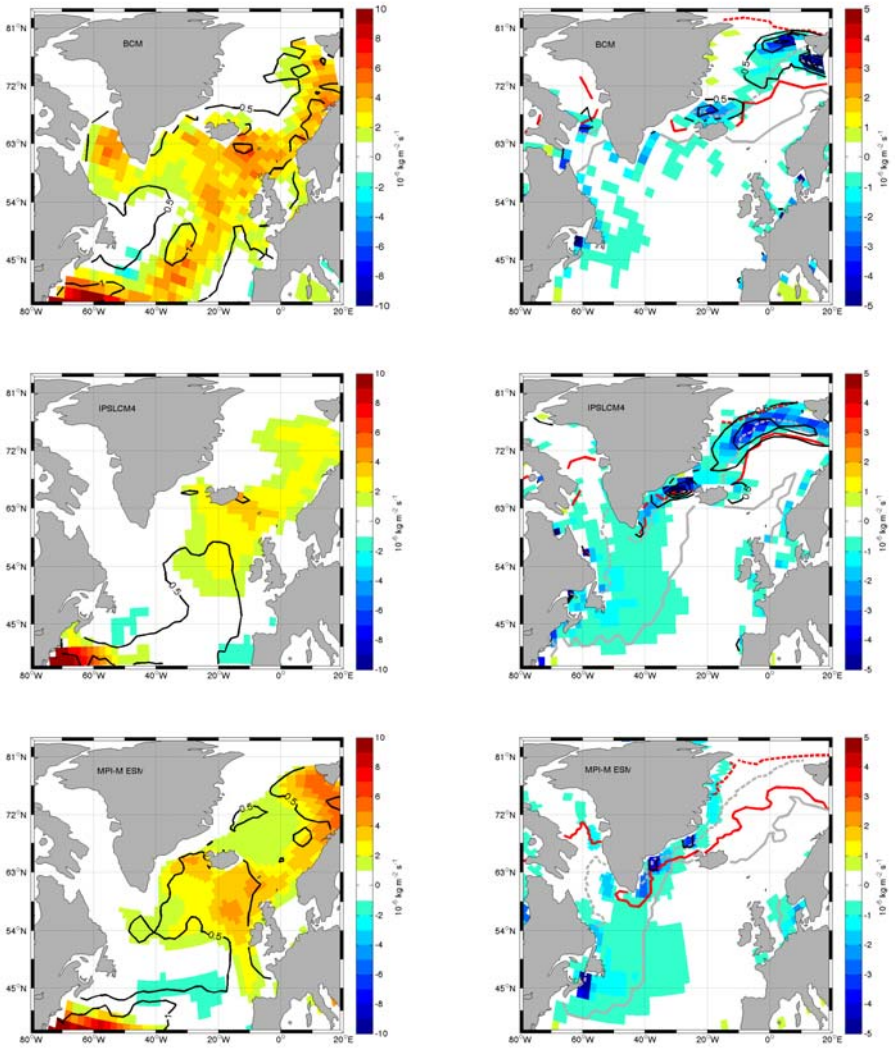

Figure 3.6: The thermal (left; F_T) and haline (right; F_S) contribution to the annual mean density flux into the ocean for the different models, given in 10^{-6}*kg m^{-2} s^{-1}. Positive values indicate densification. Model names are indicated in the upper left corner of the figures. Note the different scales on the colorbars between F_T and F_S, and that ice melting/freezing is not taken into account in the F_S for MPI-M ESM. One standard deviation of the interannual variability of F_T and F_S are shown by black contours with intervals of 0.5. The red solid (dashed) lines indicate maximum (minimum) sea ice extent in September. Likewise for the grey lines, but for March.

3.2 AMOCz versus AMOCσ

The strength and structure of the overturning circulation in latitude-depth space, i.e., AMOCz is shown in Fig. 3.7 (left panel). The BCM and MPI-M ESM have comparable maximum value of the AMOCz (17.9 Sv and 15.2 Sv, respectively, at 35.5°N), while the maximum value for IPSLCM4 is about half of that (9.6 Sv at 44°N). The maximum values of the AMOCz are located at 1000 m, 1020 m, and 1406 m in BCM, MPI-M ESM, and IPSLCM4 respectively.

To emphasize the gradual densification of the Subtropical Water, AMOCσ (Fig. 3.7, right panel) is presented for the same region as AMOCz. The density bins chosen for the computation of AMOCσ in IPSLCM4 and MPI-M ESM are consistent with the isopycnal discretization of the ocean model in BCM. The WMT from lighter to denser water masses of the poleward flowing water is evident in all models considered here, although their strengths and pattern differ. The WMT in BCM occurs over a broad density range compared to that in IPSLCM4 and MPI-M ESM. North of 50°N, the isolines of the overturning streamfunction incline from low to high densities in the density range of Subpolar Mode Water. The density of the surface flow increases also south of 50°N in BCM, whereas there is less densification (i.e., less sloping) in IPSLCM4 and MPI-M ESM in this region.

Assessing the overturning circulation in latitude-density space captures the densification with the essentially horizontal Subpolar Gyre circulation (Fig. 3.4). This leads to a stronger AMOCσ than AMOCz in the subpolar region, and in general an overturning circulation cell that extends further north. The maximum value of AMOCσ is still much lower for IPSLCM4 (9.4 Sv at 53°N) than in the two other models (18.3 Sv at 58°N and 51°N for BCM and MPI-M ESM, respectively). The maximum AMOCσ is located in a slightly less dense layer for MPI-M ESM (σ_2=36.29) compared to that of the two other models (σ_2=36.71).

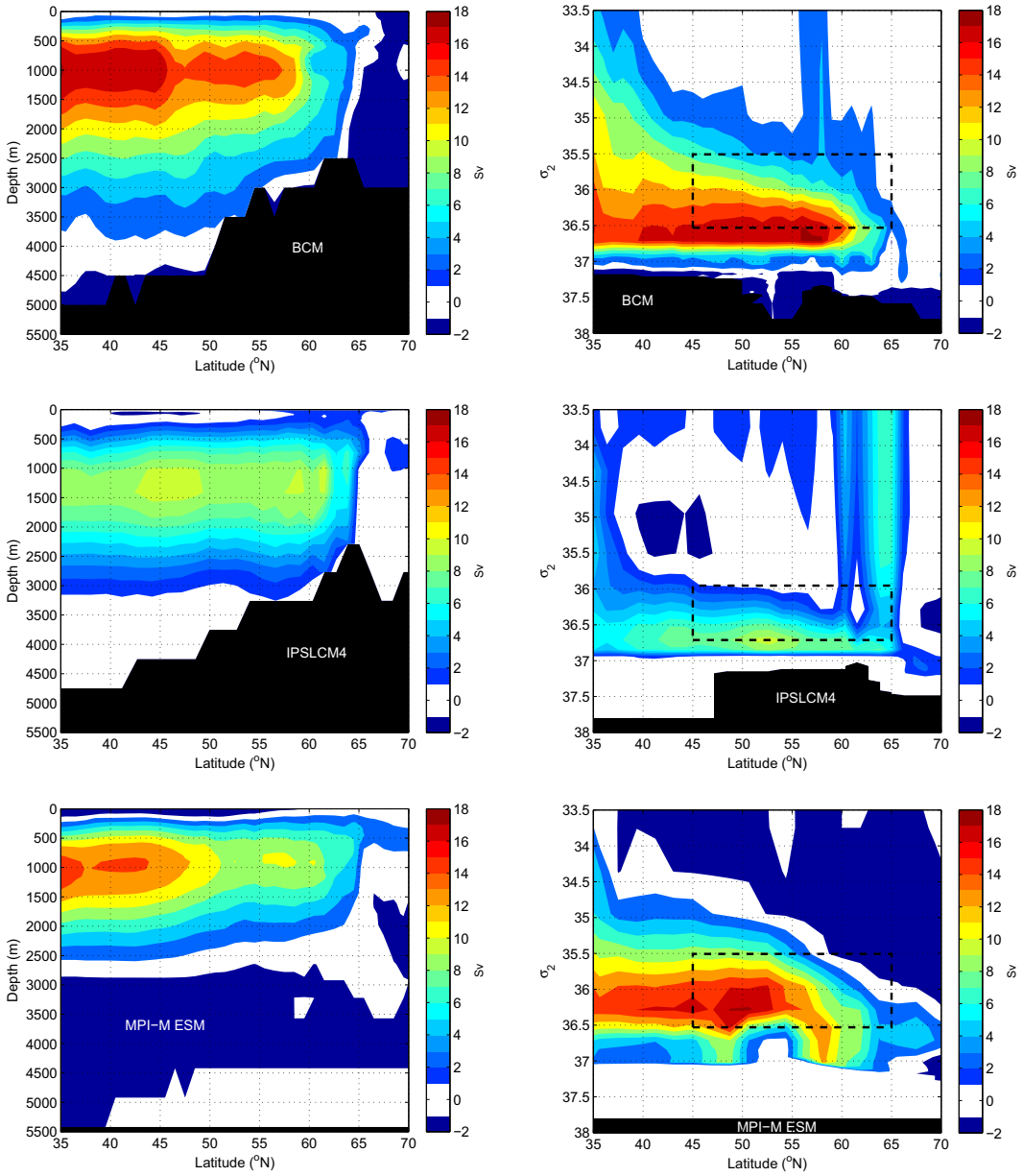

Figure 3.7: Meridional overturning streamfunction in latitude-depth space (AMOCz; left) and latitude-density space (AMOCσ; right) for the different models. Model names are indicated in the figures. The dashed rectangles illustrate the approximate density range of the model's Subpolar Mode Water in the latitude band from 45°N to 65°N.

3.3 Surface-forced water mass transformation in the eastern subpolar North Atlantic

While AMOCσ quantifies zonally averaged WMT from the actual isopycnal transports, the approach of Walin (1982) estimates the geographical distribution of WMT from the surface density fluxes and hydrography in outcrop regions (Fig. 3.3a; cf. 2.3). The density range investigated for each model is defined by the isopycnals that outcrop in the eastern subpolar region (Fig. 3.3b).

Brambilla et al. (2008) have done an extensive observation-based analysis on the WMT of Subtropical Water and subsequent formation of Subpolar Mode Water in the northeastern North Atlantic (Fig. 3.8). We have applied the same methodology as Brambilla et al. (2008), and their observation-based WMT therefore provides a benchmark for assessing model performance in this particular region. The WMT of the models and the observation-based WMT are intercompared according to two criteria: WMT structure and density range. The magnitude of the WMT cannot be compared, since the horizontal resolution of the models and the observation-based data differs, but our focus is on WMT structure. To further look at the quantitative WMT of the models, the magnitude of the *integrated* WMT in the eastern subpolar region is compared at the end of this section.

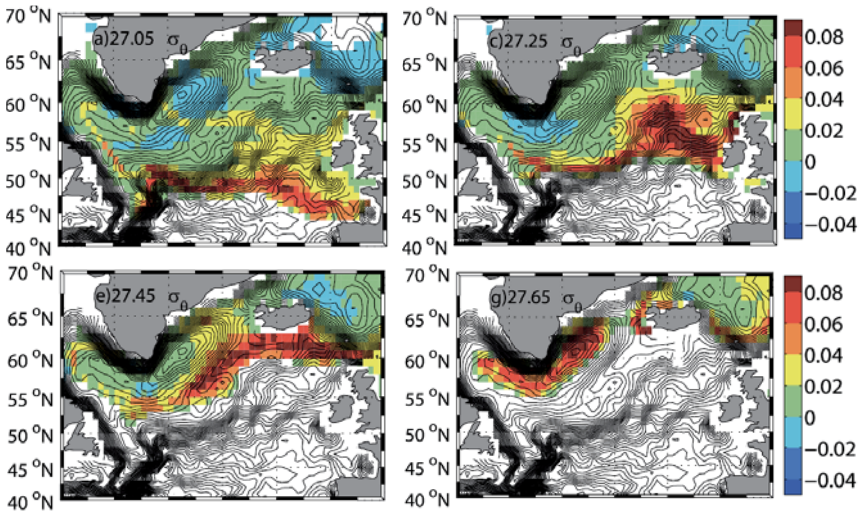

Figure 3.8: Observation-based annual mean surface forced water mass transformation (Sv) is shown in color. The corresponding density is noted in the figures. Positive values denote densification. Values are plotted on a regular 1° x 1° grid. The black lines are the surface flow streamlines. Figure 4 in Brambilla et al. (2008).

In BCM the structure of the WMT for four different densities (Fig. 3.9) are in qualitative agreement to those obtained from the observation-based study. Several branches of strong WMT with distinct densities are associated with different classes of Subpolar Mode Water. The BCM has strong WMT from Cape Cod and towards the northeastern North Atlantic. This is in accor-

dance with the observation-based WMT. However, the position of the North Atlantic Current differs between BCM and the observation-based estimates (Fig. 3.8; see also Krauss 1986; Pérez-Brunius et al. 2004), thereby giving somewhat different regions of strong WMT. The BCM is nevertheless more similar to the observation-based WMT in this aspect than the other two models. The North Atlantic Current is observed to curve around Newfoundland before it turns northeastward in the "Northwest Corner" (e.g., Arhan 1990). In BCM on the other hand, the North Atlantic Current turns northeastward already south of Newfoundland (cf. Fig. 3.4; see also Langehaug et al., in revision, for more details). In BCM, the WMT occurs for densities comparable to the observation-based WMT (Fig. 3.9), but for slightly lighter water masses. The densities of BCM's Subpolar Mode Water are captured by the four lightest densities shown in Fig. 3.3b, which is probably due to a warm bias of the ocean surface in the North Atlantic region compared to observations (Otterå et al. 2009).

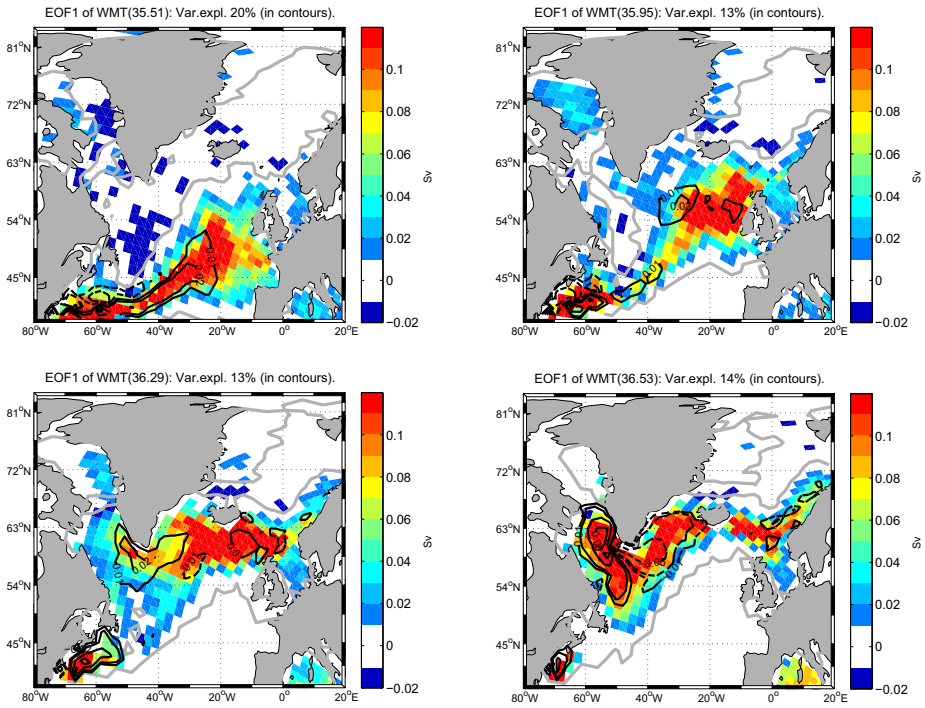

Figure 3.9: BCM's annual mean surface-forced water mass transformation (WMT) is shown in color. The corresponding σ_2-density is noted in the title of the figures. Positive values denote densification. The grey line indicate the zero line for the annual mean WMT. EOF1 of the WMT is shown in contours with intervals of 0.03 Sv, starting from $\pm$0.02 Sv. Contours for $\pm$0.01 Sv are also shown. Solid (dashed) lines indicate positive (negative) values. The variance explained by EOF1 of the total variability in the WMT is given in the title of the figures.

In IPSLCM4, the WMT shows a different structure than both BCM and the observation-based WMT (Fig. 3.10). IPSLCM4 shows strong WMT just south of Newfoundland, but between

this region and the northeastern North Atlantic the WMT is weak with values lower than 0.01 Sv. In the southern subpolar region the weak WMT could be due to the excessive amount of freshwater in this region mentioned above (see the negative surface density flux in Fig. 3.6), preventing outcropping of the same isopycnals that outcrop in the northeastern North Atlantic. In the vicinity of the Greenland-Scotland Ridge the structure of the WMT in IPSLCM4 is more similar to BCM and the observation-based WMT, where distinct densities are related to different branches of strong WMT. In IPSLCM4 the WMT occurs for densities comparable to the observation-based WMT, but for slightly denser water masses than in BCM. This might be due to a cold bias of the IPSLCM4 at middle to high latitudes (Marti et al. 2010).

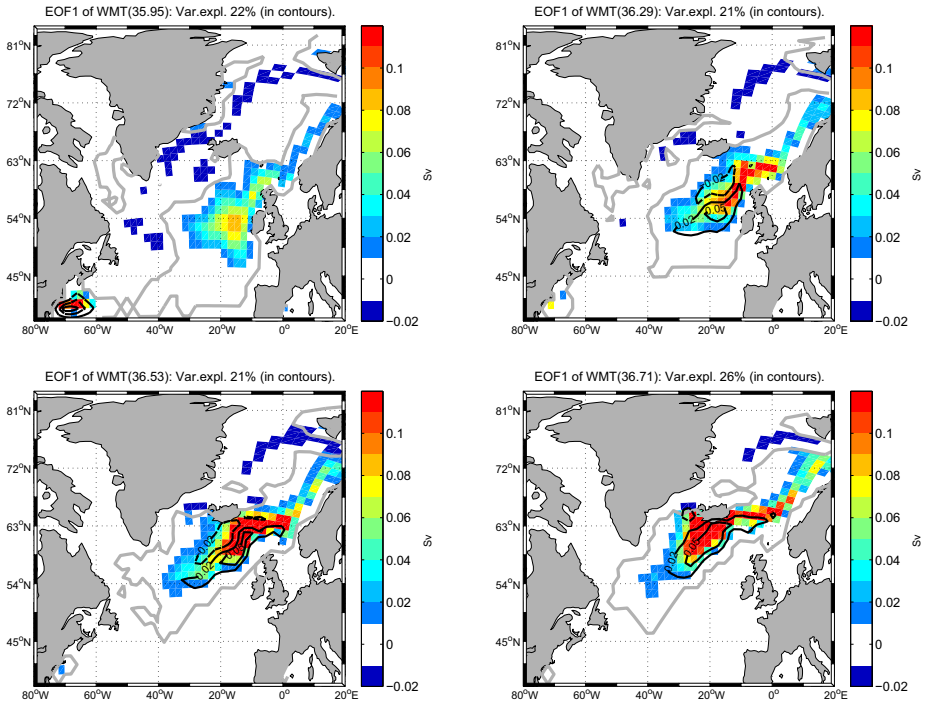

Figure 3.10: IPSLCM4's annual mean surface-forced water mass transformation (WMT) is shown in color. The corresponding σ_2-density is noted in the title of the figures. Positive values denote densification. The grey line indicate the zero line for the annual mean WMT. EOF1 of the WMT is shown in contours with intervals of 0.03 Sv, starting from $\pm$0.02 Sv. Solid (dashed) lines indicate positive (negative) values. The variance explained by EOF1 of the total variability in the WMT is given in the title of the figures.

The MPI-M ESM displays a different WMT structure than both the other two models and the observation-based estimate (Fig. 3.11). Here WMT mainly occurs along the eastern boundary of the North Atlantic Basin and the Nordic Seas. This is consistent with the very zonal North Atlantic Current in MPI-M ESM, crossing the entire basin before continuing north (Fig. 3.4). Similar to IPSLCM4, MPI-M ESM has strong WMT just south of Newfoundland and weak

WMT in the southern subpolar region. The WMT for the lightest density becomes negative east of Newfoundland (upper left panel in Fig. 3.11). This means that the surface water becomes less dense here, which is consistent with the negative contribution to the annual mean density flux both from the thermal and haline component in this region (Fig. 3.6). This is also the case in IPSLCM4 (upper left panel in Fig. 3.10). In MPI-M ESM the WMT occurs for the same densities as in BCM.

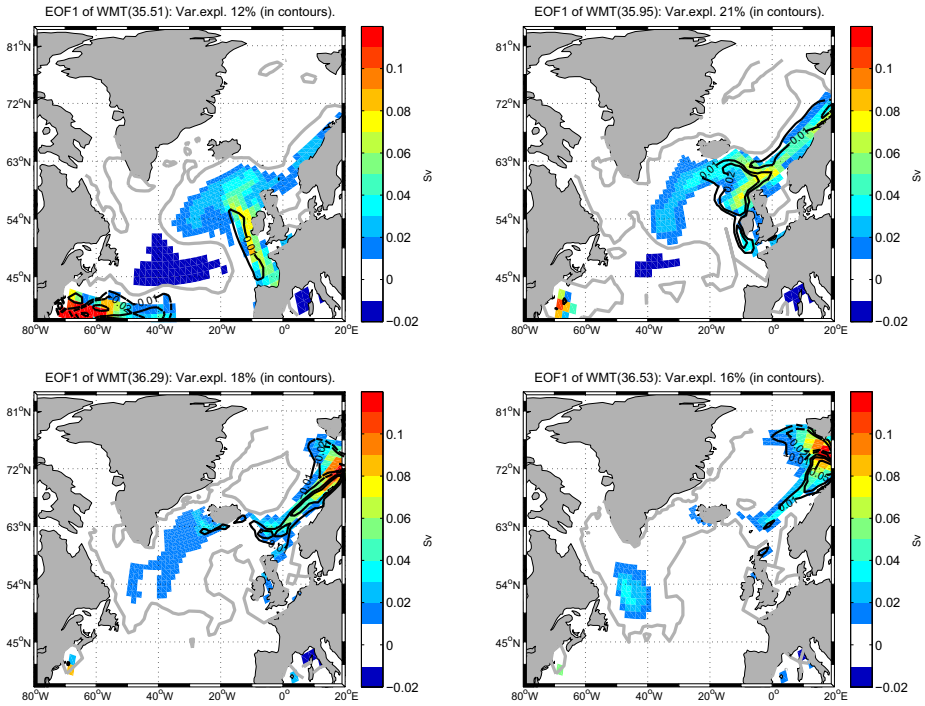

Figure 3.11: MPI-M ESM's annual mean surface-forced water mass transformation (WMT) is shown in color. The corresponding σ_2-density is noted in the title of the figures. Positive values denote densification. The grey line indicate the zero line for the annual mean WMT. EOF1 of the WMT is shown in contours with intervals of 0.03 Sv, starting from $\pm$0.02 Sv. Contours for $\pm$0.01 Sv are also shown. Solid (dashed) lines indicate positive (negative) values. The variance explained by EOF1 of the total variability in the WMT is given in the title of the figures.

To locate where most of the WMT occurs and to allow for quantitative comparison of the magnitude of the WMT among the models, the integrated WMT of the entire subpolar North Atlantic and the eastern subpolar region (48-62°N and east of 35°W) are shown for the whole density range (Fig. 3.12). For IPSLCM4 and MPI-M ESM, nearly all of the WMT in the subpolar region occurs in the eastern part, east of 35°W. This is also the case for BCM for $\sigma_2 \leq 35.95$, but the WMT in the western part contributes with a substantial amount of the denser WMT (cf. Fig. 3.9).

This graphic also shows that the integrated WMT in the subpolar region is generally stronger in BCM than in the other two models (Fig. 3.12). The maximum integrated WMT in the subpolar region in BCM (12.7 Sv) is 72% of the northward flow at the entrance to the subpolar region (Table 3.2). This means that the surface water in the subpolar region is not transformed at the same rate as the incoming transport of Subtropical Water. In IPSLCM4 and MPI-M ESM the fraction of transformed surface water in the subpolar region is even less, and is at maximum 57% and 40%, respectively, of the incoming transport of Subtropical Water (Table 3.2). However, the isopycnals that outcrop in the subpolar region also outcrop in neighboring seas, such as the Nordic Seas (see Fig. 3.9, 3.10, and 3.11). Hence, part of the "missing" transformation takes place in neighboring seas. Particularly MPI-M ESM has large WMT close to Svalbard.

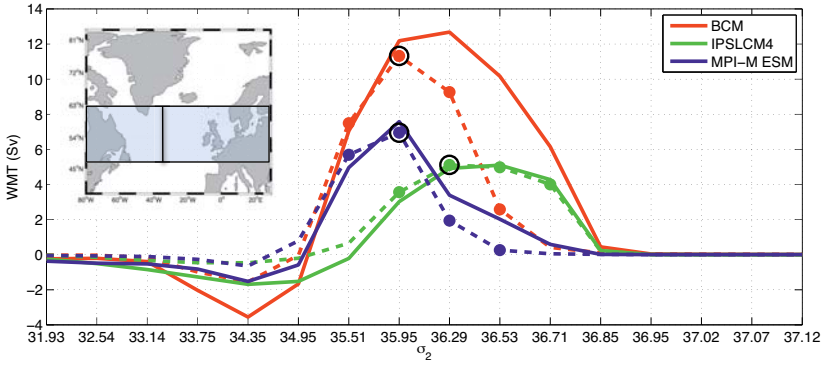

Figure 3.12: Annual mean surface-forced water mass transformation (WMT) as a function of density, integrated over the entire subpolar region (48°N-62°N as indicated in the inset; solid lines) and over the eastern subpolar region (east of 35°W; dashed lines). Filled circles indicate the integrated WMT for the densities shown in Fig. 3.9, 3.10, and 3.11. The density associated with the strongest WMT is indicated with a black circle, and the time series of this WMT is shown in Fig. 3.14 for the different models.

Table 3.2

Northward volume transport (in Sv) obtained from AMOCσ at the southern (48°N) and northern (60-64°N) boundary of the subpolar region.

	BCM	IPSLCM4	MPI-M ESM
Southern	17.6	8.9	18.9
Northern	9.9	6.8	8.7

3.4 Comparing isopycnal transport and surface-forced water mass formation

To investigate how the surface-forced WMT according to the approach of Walin (1982) represents the actual WMT in the models, we compare the estimated surface-forced formation (cf. Section 2.3) and isopycnal transports obtained from AMOCσ (Fig. 3.7, right panel). The surface-forced formation is calculated for all isopycnals that outcrop in the region between 48°-62°N. The surface-forced forced formation has a similar structure in all models, i.e., removal of water with lighter densities and accumulation of water with denser densities (Fig. 3.13). The difference in the isopycnal transport between the northern (48°N) and southern (62°N) boundary of the subpolar region corresponds well with the estimated surface-forced formation in IPSLCM4 and MPI-M ESM, but less well for BCM (Fig. 3.13).

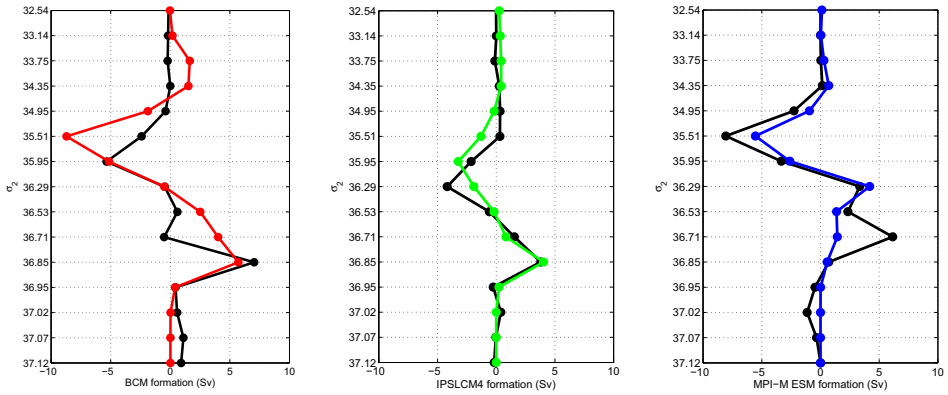

Figure 3.13: Annual mean surface-forced water mass *formation* integrated over the subpolar region (colored lines; derivatives with respect to density of the solid curves in Fig. 3.12). The region is indicated in the inset in Fig. 3.12. The net isopycnal volume transport through the subpolar region (black lines) is found by subtracting the transport profile in density bins at 48°N from the transport profile in density bins at 62°N.

One reason for the difference between the surface-forced formation and net isopycnal transport through the subpolar region in BCM is the model parameterization of deep convection: whenever the water column is unstable, such as for instance in the Labrador and Irminger seas, there is an instantaneous re-stratification of the water column and thickening of the denser layers (Medhaug et al. 2011). Due to this instantaneous re-stratification at each time step in the model simulation, there is no outcropping in our diagnosis associated with this process. This means that parts of the water that are accumulated in the isopycnal layers with densities σ_2 = 36.53 and σ_2 = 36.71 (red curve in Fig. 3.13) are in BCM placed in denser layers by deep convection (black curve in Fig. 3.13).

An additional contribution is mixing. It should therefore not be a perfect match between the surface-forced formation and the net isopycnal transport through the subpolar region. For in-

stance, the surface-forced formation in MPI-M ESM cannot explain the positive isopycnal flow with density σ_2 = 36.71 (black curve in Fig. 3.13). In BCM, the separate mixed layer makes the dynamics of the upper ocean in BCM different from the other two models. For instance, vertical mixing is implicit to the model formulation, for the model mixed layer to be vertical homogenous at all times (Eldevik 2002). Nurser et al. (1999) used an isopycnal model to investigate the contribution from mixing on the total WMT in the North Atlantic Ocean. Mixing was found to reduce the effect of the surface-forced WMT. In the upper layers of BCM the magnitude of the estimated surface-forced formation is larger than the net isopycnal transport through the subpolar region (Fig. 3.13). This may therefore be attributed to the fact that we have not included mixing as a source for WMT in our analysis.

4. Decadal variability

Several model studies have shown that decadal climate variations are linked to variations of AMOC (Eden and Willebrandt 2001; Bentsen et al. 2004; Deshayes and Frankignoul 2008). In this section, we thus investigate the variability of the WMT and its link with decadal variability of the AMOCσ.

4.1 Surface-forced water mass transformation in the eastern subpolar North Atlantic

The dominant patterns of WMT variability are included in Fig. 3.9, 3.10, and 3.11. In BCM the dominant Empirical Orthogonal Function (EOF) pattern for the two lighter densities show strongest variability along the pathway of the North Atlantic Current from Cape Hatteras to Ireland, whereas the dominant pattern for the two denser densities show strongest variability mainly in the Labrador and Irminger seas (Fig. 3.9). The densest density is associated with a dipole pattern with anomalous strong WMT in the Labrador Sea and anomalous weak WMT in the Irminger Sea. The leading mode and associated magnitude shown in Fig. 3.9 is generally less than the annual mean WMT. Since the annual mean WMT is mostly positive in the regions with pronounced variability, the northward flowing water becomes generally denser in these regions. The principal components of the dominant modes for three lighter densities are largely fluctuating in phase. On the other hand, the principal components for the lightest and densest density have significant, but low, positive correlation. This implies that the variability of WMT in the eastern subpolar region, associated with the inflow of Subtropical Water, differs from the variability of the WMT in the Labrador and Irminger seas (lower right panel in Fig. 3.9).

In IPSLCM4 the strongest WMT variability is mainly confined between Iceland and the British Isles, and extends into the Nordic Seas (Fig. 3.10). The leading mode and associated magnitude shown in Fig. 3.10 is generally less than the annual mean WMT similarly to BCM, reflecting that the northward flowing surface water becomes denser in the northeastern North Atlantic. The dominant modes for σ_2 = 36.29 and σ_2 = 36.53 constitute a zonal dipole pattern. The principal components of the dominant modes are largely fluctuating in phase, except for the principal component for the lightest density. This principal component has no significant correlation with

the other principal components, due to its relatively less variability in the northeastern North Atlantic (upper left panel in Fig. 3.10).

In MPI-M ESM the strongest WMT variability is found between Iceland and the British Isles and along the eastern rim of the Nordic Seas (Fig. 3.11). Similar to IPSLCM4, the variability of the WMT for the lightest density is low. The dominant modes for the two denser densities are characterized by a meridional dipole pattern; when there is anomalous strong WMT in the Norwegian Sea, there is anomalous weak WMT close to Svalbard (lower panels in Fig. 3.11). Similarly to the other two models, the leading mode and associated magnitude shown in Fig. 3.11 is generally less than the annual mean WMT. The principal components of the dominant modes have high lagged correlation, except for the principal component for the lightest density. For instance, the dominant mode with increased WMT (for σ_2 = 35.95) to the north of the British Isles leads the dominant mode with increased WMT (for σ_2 = 36.53) close to Svalbard with a time lag of about two years.

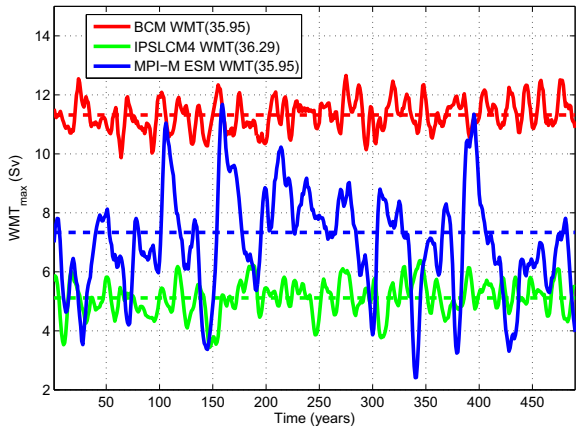

Figure 3.14: Surface-forced water mass transformation integrated over the eastern subpolar region (48^{o}N-62^{o}N, east of 35^{o}W, as indicated in the inset in Fig. 3.12) for the σ_2-densities indicated in the legend for the different models. These densities correspond to the maximum WMT for the different models (shown in Fig. 3.12). The time series are filtered using a 11-year low-pass filter. The dashed lines illustrate the mean integrated WMT for each model.

There is no common pattern in the variability of the WMT among the models, according to the EOF analysis above, except that the strongest variability is found in the regions with largest annual mean WMT. In Section 3.3 we demonstrated that the geographical distribution of the annual mean WMT differ among the models. However, all models agreed on positive WMT in the northeastern North Atlantic. In the following, the maximum WMT (WMTmax) in the eastern subpolar region (indicated by black circles in Fig. 3.12) is used to represent the decadal variability of the WMT associated with Subpolar Mode Water (Fig. 3.14). In IPSLCM4 and

MPI-M ESM the correlation is high between WMTmax and the principal components of the dominants mode shown in Fig. 3.10 and 3.11 (Table 3.3). In BCM the correlation is significant, but low. The dominants modes for IPSLCM4 and MPI-M ESM are mainly confined to the northeastern North Atlantic, whereas those for BCM cover a broader region. This partly explains the lower correlation in BCM.

Table 3.3

Peak correlations (r) within time lags of -5 and +5 years between the maximum WMT in the eastern subpolar region (WMT_{max}, shown in Fig. 15) and the first principal components (PC1) of the WMT across the different σ_2-isopycnals ($\sigma1$-$\sigma4$). WMT_{max} leads for positive lags. Time series are filtered using a 11-year low-pass filter.

	BCM WMT_{max}		**IPSLCM4** WMT_{max}		**MPI-M ESM** WMT_{max}	
	r	lag	r	lag	r	lag
PC1 of WMT($\sigma1$)	0.24	1	-	-	0.49	1
PC1 of WMT($\sigma2$)	0.31	1	0.83	2	0.97	1
PC1 of WMT($\sigma3$)	0.30	0	0.79	3	0.92	3
PC1 of WMT($\sigma4$)	0.44	-1	0.72	3	0.86	3

4.2 Relationship between AMOCσ and surface-forced water mass transformation variability in the eastern subpolar North Atlantic

The dominant patterns of AMOCσ variability for each model are shown in Fig. 3.15 (left panel). In BCM and MPI-M ESM the dominant mode shows mainly a strengthening of the southward flow in the dense layers and a slightly weakening of the mass flux in lighter layers. Unlike AMOCz, variability in AMOCσ can also be related to changes in thickness of the isopycnal layers. For instance, if the thickness of a dense layer increases, the thickness of lighter layers decreases. In other words, a reorganization of the water masses in the water column, which could be caused by deep convection. This reorganization does not necessary give a larger net southward volume flux. The dominant mode of AMOCσ indicates that there is strong variability in the dense layers, either due to changes in layer thickness, or a combination of changes in thickness and velocity. Therefore, there can be a strengthening of the deep flow without an immediate strengthening of the surface flow.

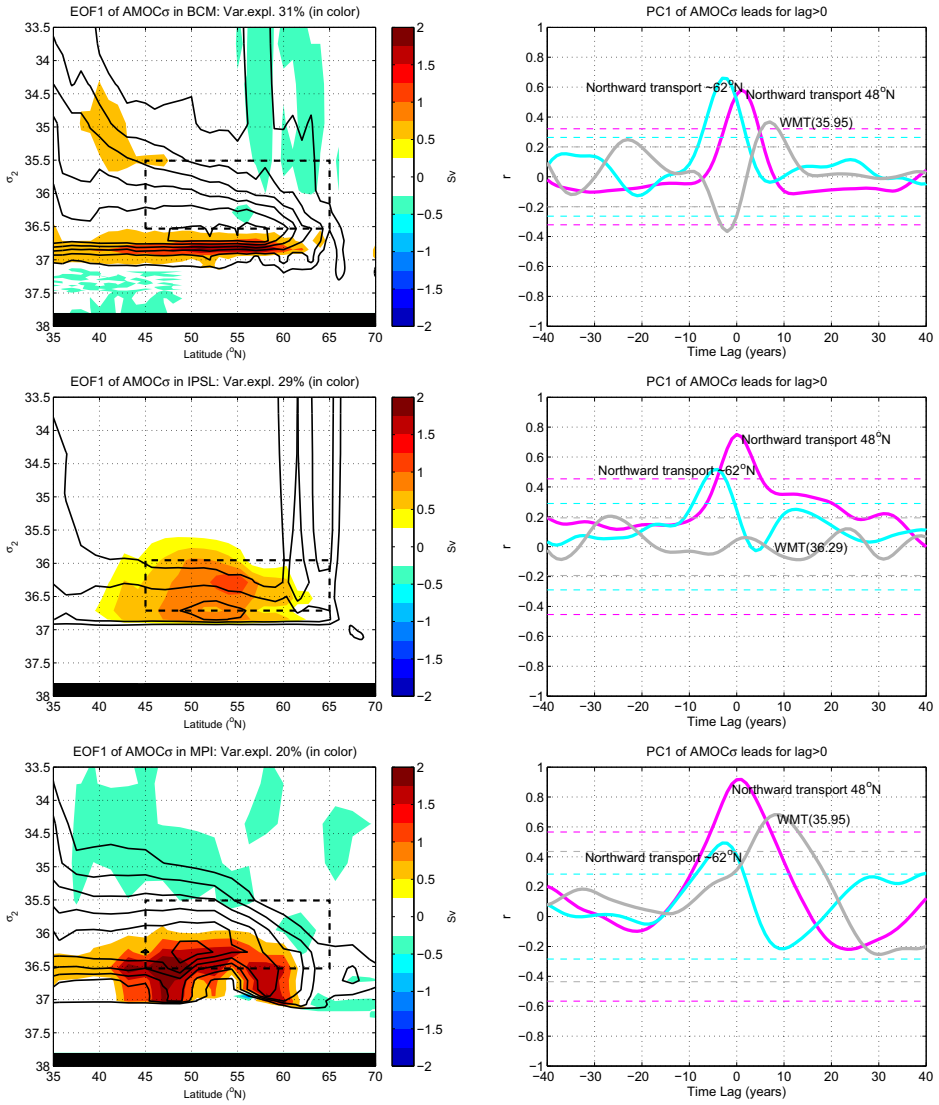

Figure 3.15: Left panel: EOF1 of AMOCσ is shown in color for the different models. Model names and the variance explained by EOF1 of the total variability in AMOCσ is indicated in the title of the figures. Mean AMOCσ is shown in contours with intervals of 3 Sv. The dashed rectangles illustrate the approximate density range of the model's Subpolar Mode Water in the latitude band from 45°N to 65°N. Right panel: Cross-correlation (r) between PC1 of AMOCσ and 1) net northward volume transport at 48°N, 2) mean net northward transport between 60-64°N, and 3) surface-forced water mass transformation (WMT) integrated over the eastern subpolar region for the σ_2-densities indicated in the figures. These densities correspond to the maximum WMT for the different models (shown in Fig. 3.12). PC1 of AMOCσ leads for positive time lags, as indicated in the title of the figures. The time series are filtered using a 11-year low-pass filter.

The northward flow at 48°N is found to increase one year after the southward flow in the dense layers strengthens (Table 3.4 and magenta curves in Fig. 3.15). Similar results have been shown by Grist et al. (2009), although in a somewhat different way. They investigated the total surface-forced WMT north of 48°N. Their WMT therefore includes the formation of the densest water masses in the Nordic Seas and Labrador and Irminger seas, and is thus possibly more related to the variability of the dense southward flow. This corresponds to our dominant mode of AMOCσ (Fig. 3.15). A main finding from Grist et al. (2009) is that increased formation of dense water masses at northern high latitudes leads to lagged increase in the northward flow at 48°N (i.e., an increase in the maximum AMOCz at 48°N). In IPSLCM4 the dominant mode shows a strengthening of the entire AMOCσ, where the northward flow at 48°N increases at zero time lag (Table 3.4 and Fig. 3.15).

Table 3.4

Peak correlations (r) and corresponding time lag (in years) between the first EOF of AMOCσ and the northward volume transport at the southern (48°N) and northern (60-64°N) boundary of the subpolar region, and the maximum WMT in the eastern subpolar region (WMT_{max}, shown in Fig. 15). AMOCσ leads for positive lags. Time series are filtered using a 11-year low-pass filter.

	BCM AMOCσ		**IPSLCM4** AMOCσ		**MPI-M ESM** AMOCσ	
	r	lag	r	lag	r	lag
Northern	0.66	-3	0.52	-4	0.49	-3
Southern	0.58	1	0.75	0	0.92	1
WMT_{max}	-0.37/0.37	-2/7	-	-	0.68	8

To investigate the decadal relationship between WMT associated with Subpolar Mode Water and AMOCσ, the WMTmax (shown in Fig. 3.14) has been correlated with the first principal component of AMOCσ. In BCM and MPI-M ESM the two have a significant correlation, where the WMTmax is found to lag AMOCσ (Table 3.4 and grey curves in Fig. 3.15). This means that 7-8 years after an increase in the southward flow of dense water masses in the North Atlantic Basin there is an increase in the WMT, and hence, the heat loss in the eastern subpolar region. Gastineau and Frankignoul (2011) used the same model simulations as presented in this study, among others, and found that an intensification of AMOCz was followed by low sea level pressure anomalies over the North Atlantic, with a time lag of 1-10 years. They found that this atmospheric response was caused by increased northward oceanic heat transport, resulting in increased heat release along the pathway of the North Atlantic Current. These results are consistent with the results from BCM and MPI-W ESM in this study.

In IPSLCM4 there is no significant correlation between the WMTmax and AMOCσ (Table 3.4 and Fig. 3.15), although the mechanism discussed above is also found in IPSLCM4 in the study by Gastineau and Frankignoul (2011). The reason is that the latter study focuses on a broader region, and therefore captures the increased heat loss in the subtropical region. In this study we only investigate changes in the eastern subpolar region, where there is no significant increase in the heat loss. This is consistent with Gastineau and Frankignoul (2011). The reason for this difference in IPSLCM4 compared to the other models could be related to the anomalously cold and fresh surface layer in the southern subpolar region (Fig. 3.5). The North Atlantic Current subducts beneath this layer, where its positive sea surface temperature anomalies could be eroded, before it enters the eastern subpolar region. In MPI-M ESM there is also a cold and fresh surface layer in the southern subpolar region (Fig. 3.5). However, the North Atlantic Current has a more zonal pathway in this model (Fig. 3.4), omitting the cold and fresh surface layer spreading eastward from Newfoundland.

If we move further north and investigate the relationship between the northward transport at 60-64°N and the first principal component of AMOCσ, a strengthening of the former is found to lead an increase in AMOCσ (Table 3.4 and blue curves in Fig. 3.15). The northward transport at 60-64°N represents mainly the inflow into the Nordic Seas. This suggests a key role for the light-to-dense water transformation in the Nordic Seas in the strengthening of the southward dense flow in the North Atlantic Basin. The northward transport both at 48°N and 60°-64°N is shown in Fig. 3.16. The variability of the northward transport at 60-64°N in MPI-M ESM (one standard deviation is 1.8 Sv) is about two times larger than for the other two models (0.5 Sv). The mean ratio of the northward transport at 60°-64°N to the northward transport at 48°N is 57%, 76%, and 47% for BMC, IPSLCM4, and MPI-M ESM, respectively. In BCM and MPI-M ESM, about half of the northward flow at 48°N re-circulate in the western subpolar region, while about a quarter re-circulates in IPSLCM4. The bifurcation of the North Atlantic Current continuing into the Nordic Seas and the Labrador Sea is an important factor in setting the regions of dense water formation, and hence the composition of the North Atlantic Deep Water. In IPSLCM4 there is WMT in the Nordic Seas but weak and slightly negative WMT in the Labrador Sea (Fig. 3.10), whereas in MPI-M ESM there is positive WMT in the vicinity of the Labrador and Irminger seas, although not as strong as in the Nordic Seas. In BCM there is WMT in both the Nordic Seas and the Labrador and Irminger seas, with particularly strong WMT in the Labrador Sea.

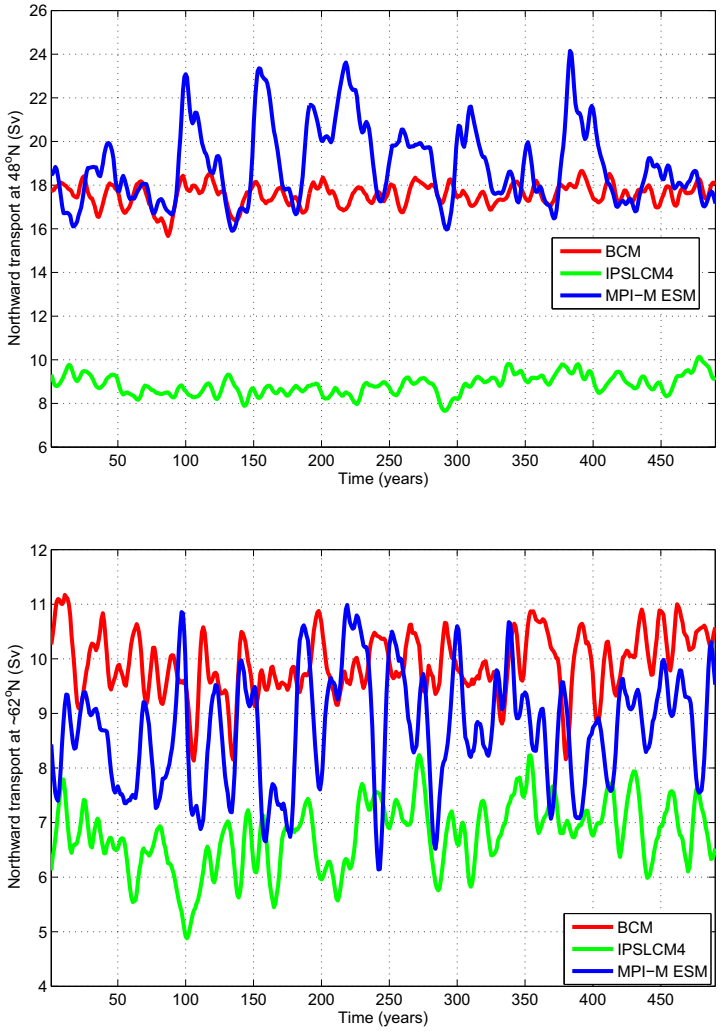

Figure 3.16: Northward transport at 48°N (upper) and 60-64°N (lower). The northward transports are the integrated positive volume transport in density space. The time series are filtered using a 11-year low-pass filter.

5. Summary and Concluding remarks

In this study we have analyzed three 500-year long climate model simulations of a pre-industrial climate. The focus has been on the mean state and decadal variability of the North Atlantic Current and WMT associated with Subpolar Mode Water. The model intercomparison reveals both similarities and differences in the geographical distribution of WMT. One similarity is that heat loss dominates WMT in the eastern subpolar region, considering both the mean state and variability (Fig. 3.6). The dominance of the thermal contribution over the haline contribution in the subpolar region is also found in a study using both a high- and coarse resolution ocean model forced with ERA15 reanalysis data (Gulev et al. 2007). In addition, all models show that the main part of the WMT in the subpolar region occurs in the eastern part (east of 35°W; Fig. 3.12).

Among the three models, the mean WMT in BCM is most comparable to the observation-based mean WMT (Fig. 3.8 and 3.9; Brambilla et al. 2008), since it appears to have the more realistic structure of the North Atlantic Current. The other two models differ from the observation-based WMT in the southern subpolar region and in the Labrador Sea (Fig. 3.10 and 3.11). In IPSLCM4 the barotropic circulation is weaker than in the two other models (Fig. 3.4), the North Atlantic Current subducts in the southern subpolar region, and a quarter of northward flow at 48°N is estimated to re-circulate in the western subpolar region. The pathway and strength of the North Atlantic Current in IPSLCM4 could be related to the excessive sea ice extent in the Labrador Sea (Fig. 3.6). In MPI-M ESM, the North Atlantic Current crosses the entire North Atlantic Basin before continuing north (Fig. 3.4). Even though about half of the model's northward flow at 48°N is estimated to re-circulate in the western subpolar region, the heat carried by the current is not sufficient to keep the sea ice from advancing south (Fig. 3.6). Hence, similarly to IPSLCM4, the excessive sea ice extent could be related to the pathway of the North Atlantic Current.

Since the WMT is weak in the southern subpolar region and the Labrador Sea in IPSLCM4 and MPI-M ESM, the magnitude of the integrated WMT in the subpolar region is larger in BCM than in the two other models. In addition, the magnitude of the WMT in the eastern subpolar region is large in BCM compared to the other two. This is both due to stronger heat loss and less freshwater input than in IPSLCM4 and MPI-M ESM in this region (Table 3.1). The magnitude of the spatially integrated WMT varies with respect to density in all models (Fig. 3.12). The maximum WMT in the eastern subpolar region for BCM, IPSLCM4, and MPI-M ESM is 11 Sv, 7 Sv, and 5 Sv, respectively.

An important result from this study is that the pathway of the North Atlantic Current, and hence the northern WMT, can be quite different between two models despite of a similar AMOCz. The structure of the AMOCz in BCM and MPI-M ESM are comparable, and they have a similar maximum strength of about 18 Sv (Fig. 3.7). However, the above discussion demonstrates that there are several important differences between these two models in the northern North Atlantic. It is thus necessary to apply additional analysis complimentary to the frequently used

AMOCz. One way of assessing the *zonally* averaged WMT is to use AMOCσ. For instance, the weak WMT in the southern subpolar region in IPSLCM4 and MPI-M ESM compared to BCM is also evident from comparing AMOCσ from the models (Fig. 3.7). The maximum AMOCσ for the different models are similar to the values obtained from AMOCz, although the maxima are shifted towards the subpolar region. On the other hand, AMOCσ does not provide information on the pathway of the North Atlantic Current. For instance, in IPSLCM4 the WMT is weak due to subduction of the North Atlantic Current, and hence, there is little heat loss in this region (Fig. 3.5). In MPI-M ESM the WMT is weak in the subpolar region due to a balance of buoyancy gain in the western part and buoyancy loss (heat loss) in the easternmost part (Fig. 3.6). Thus, the models appear to be similar, but are similar for the wrong reasons. It therefore seems important to investigate the geographical distribution of WMT. The method introduced by Walin (1982) provides a simple and useful way of assessing WMT in climate models. However, the most accurate description of WMT associated with the overturning circulation in climate models would be from two-dimensional fields of diapycnal mixing and diapycnal velocity for each isopycnal layer. Unfortunately, these fields are not available model output from the model simulations used herein.

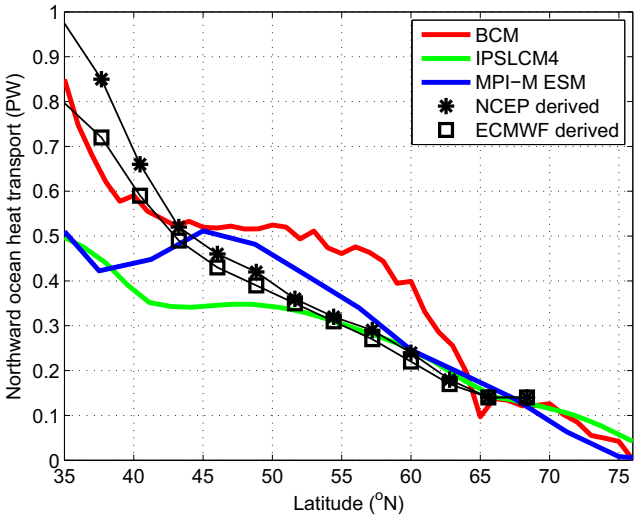

Figure 3.17: Net northward ocean heat transport in the subpolar North Atlantic for the three models. The black squares and stars denote the ocean heat transport based upon surface fluxes for 1985 to 1989 for NCEP and ECMWF reanalysis (Trenberth and Caron 2001).

WMT at northern high latitudes, particularly in the eastern subpolar region and the Nordic Seas, is highly related to ocean heat loss (Table 3.1). It is therefore useful to investigate the northward ocean heat transport in climate models, since divergence in the merdional ocean heat transport denotes regions with heat loss. The northward ocean heat transport is shown for all three mod-

els in Fig. 3.17, and is compared with observation-based estimates. It is important to note that the observation-based data contain large uncertainties. The ECMWF and NCEP derived data compare relatively well in the northern North Atlantic, but the difference between these two estimates is larger at low latitudes (Rhines et al. 2008). The divergence of ocean heat transport in BCM is particularly large between 35°-40°N and 60°-65°N, consistent with large heat loss in these regions (Fig. 3.5). Between these regions the North Atlantic Current is generally aligned with the front between subpolar and subtropical waters (Fig. 3.4), i.e., weaker heat loss occurs in this region. Also the other two models have large divergence just north of 35°N, due to large heat loss close to Cape Cod. On the other hand, between 38°-45°N there is convergence of ocean heat transport in MPI-M ESM. This is consistent with warming of the ocean surface close to Newfoundland (Fig. 3.5). In IPSLCM4 there are almost no meridional changes in the ocean heat transport between 43°-50°N, since the heat loss in the eastern subpolar region is similar to the heat gain in the western subpolar region (Fig. 3.5). It is evident that the model comparison of northward ocean heat transport highlights several differences in the location and strength of heat loss. The northward ocean heat transport has a significant impact on the North Atlantic climate (Gregory et al. 2005; Rhines et al. 2008). The impact of these model differences on their North Atlantic Climate should therefore be investigated.

In the previous section we described a mechanism where AMOCσ decadal scale variability is reflected in the variability of air-sea exchanges in the eastern subpolar region in two of the models; an increase in the southward dense flow in the North Atlantic Basin is associated with a lagged increase in the WMT in the eastern subpolar region. In BCM the dense layers in the North Atlantic Basin are filled up by overflow water from the Nordic Seas or dense water formed in the Labrador and Irminger seas. The decadal variability of Labrador Sea Water and Nordic Seas overflow are related to the first and third dominant mode of atmospheric variability, respectively, namely the North Atlantic Oscillation and the Scandinavian Pattern. The dense water formation in BCM and its link to the overturning and gyre circulations have been investigated in detail in Medhaug et al. 2011 and Langehaug et al. (in revision).

A strengthening of the overturning circulation (i.e., first EOF of AMOCz) three years after a positive phase of NAO is found in all three models but IPSLCM4 (Gastineau and Frankignoul 2011). The delayed oceanic response to positive NAO forcing has previously been investigated in BCM (Langehaug et al., in revision). Three years after high positive NAO periods there are evident changes in the northern North Atlantic, with indication of a northward shift in the North Atlantic Current, and positive temperature and salinity anomalies along the intensified path of the North Atlantic Current. The pattern of temperature anomalies resembles the WMT pattern for σ_2=35.51 (Fig. 3.9). This oceanic response to high positive NAO forcing is similar to what is found in both observation-based and model studies (Curry and McCartney 2001; Cooper and Gordon 2002; Lohmann et al. 2009).

Several recent studies investigate temperature and salinity anomalies on decadal scale in the northeastern North Atlantic (e.g., Johnson and Gruber 2007; Thierry et al. 2008; Häkkinen et

al. 2011). The mechanisms in these studies are different from the above mentioned associated with the overturning circulation. Häkkinen et al. (2011) suggest that wind-induced changes in the Subtropical and Subpolar gyres are responsible for the temperature and salinity anomalies observed in the northeastern North Atlantic. For instance, the observed recent relaxation of the gyres' circulation leads to a contraction of the Subpolar Gyre and an expansion of the Subtropical Gyre. This change in the surface circulation forms a gateway for warm and saline anomalies to propagate from the Subtropical region to the Subpolar region (see Fig. 13 in Häkkinen et al. 2011). However, the wind-driven horizontal gyres and the overturning circulation are highly interconnected. It is therefore not straightforward to understand the relationship between the overturning circulation and sea surface temperature anomalies in the northern North Atlantic. This is demonstrated in an intercomparison of all climate model simulations from IPCC AR4 (Medhaug and Furevik 2011). The study shows that the models strongly differ in their relationship between AMOCz and sea surface temperature in the North Atlantic, and hence, no consistent mechanism was found to operate in all of the models.

Although the subpolar North Atlantic Ocean is one of the most studied ocean regions, there are still challenges in understanding the variability on decadal time scale both in nature and climate model simulations. In this study all models show similar mechanisms regarding the strength of AMOCσ and northward transport at the northern and southern boundary of the subpolar region (Fig. 3.15). Two of the models show similar mechanism regarding the strength of AMOCσ and WMT in the eastern subpolar region, as discussed above. Thus, an intriguing aspect of the present study is that even if the climate models are diverging in their representation of the northern North Atlantic mean climate, they appear to an extent to show similar mechanisms on decadal time scale.

Acknowledgments

The project has been supported by the Research Council of Norway through the BIAC (HRL and TE). The research leading to these results has also received funding from the European Community's 7th framework programme (FP7/2007-2013) under grant agreement No. GA212643 (THOR: "Thermohaline Overturning - at Risk", 2008-2012; HRL, TE, JM, and KL). This publication is no. XXXX from the Bjerknes Centre for Climate Research. We thank Cecilia M. Bitz for assistance in using the water mass transformation methodology on climate model data. We also thank Iselin Medhaug, Helge Drange, and Odd Helge Otterå for comments helping to improve the manuscript.

References

Arhan, M. (1990), The North Atlantic Current and Subarctic Intermediate Water, J. Mar. Res., 48, 109-144.

Bailey, D. A., P. B. Rhines, and S. Häkkinen (2005), Formation and pathways of North Atlantic Deep Water in a coupled ice-ocean model of the Arctic-North Atlantic Oceans, Clim. Dyn., 25, 497-516.

Bentsen, M., H. Drange, T. Furevik, and T. Zhou (2004), Simulated variability of the Atlantic meridional overturning circulation. Clim. Dyn., 22, 701-720. doi:10.1007/s00382-004-0397-x.

Bleck R., C. Rooth, D. Hu, and L. T. Smith (1992), Salinity-driven thermocline transients in a wind- and thermohaline-forced isopycnic coordinate model of the North Atlantic, J. Phys. Oceanogr., 22, 1486-1505.

Bower, A. S., M. S. Lozier, S. F. Gary, and C. W. Bö ning (2009), Interior pathways of the North Atlantic Meridional Overturning Circulation, Nature, 459, 243-247.

Brambilla, E., and L. D. Talley (2008), Subpolar mode water in the northeastern Atlantic: 1. Averaged properties and mean circulation, J. Geophys. Res., 113, C04025, doi:10.1029/2006JC004062.

Brambilla, E., L. D. Talley, and P. E. Robbins (2008), Subpolar Mode Water in the northeastern Atlantic: 2. Origin and transformation, J. Geophys. Res., 113, C04026, doi:10.1029/2006JC004063.

Cerovecki, I., and J. Marshall (2008), Eddy modulation of air-sea interaction and convection, J. Phys. Oceanogr., 38, 65-83.

Chelton, D. B. (1983), Effects of sampling errors in statistical estimation, Deep-Sea Res., 30, 1083-1101.

Cooper, C., and C. Gordon (2002), North Atlantic oceanic decadal variability in the Hadley Centre coupled model, J. Clim., 15, 45-72.

Curry, R. G., and M. S. McCartney (2001), Ocean gyre circulation changes associated with the North Atlantic oscillation, J. Phys. Oceanogr., 31(12), 3374-3400.

Dengler, M., J. Fischer, F. A. Schott, and R. Zantopp (2006), Deep Labrador Current and its variability in 1996-2005, Geophys. Res. Lett., 33, L21S06, doi:10.1029/2006GL026702.

Deshayes, J., C. Frankignoul (2008), Simulated variability of the circulation of the North Atlantic from 1953 to 2003, J. Clim., 21, 4919-4933, doi:11.1175/2008JCLI1882.1.

Eden, C., and J. Willebrand (2001), Mechanisms of interannual to decadal variability of the North Atlantic circulation, J. Clim., 14, 2266-2280.

Eldevik, T. (2002), On frontal dynamics in two model oceans, J. Phys. Oceanogr., 32, 2915-2925.

Furevik, T., M. Bentsen, H. Drange, I. K. T. Kindem, N. G. Kvamstø , and A. Sorteberg (2003), Description and validation of the Bergen Climate Model: ARPEGE coupled with MICOM, Clim. Dyn., 21, 27-51, doi:10.1007/s00382-003-0317-5.

Garrett, C., K. Speer, and E. Tragou (1995), The relationship between water mass formation and surface buoyancy flux, with application to Phillips' Red Sea model, J. Phys. Oceanogr., 25, 1696-1705.

Gastineau, G., and C. Frankignoul (2011), Cold-season atmospheric response to the natural variability in the Atlantic merdional overturning circulation, Clim. Dyn., doi:10.1007/s00382-011-1109-y.

Gregory, J. M., and Coauthors (2005), A model intercomparison of changes in the Atlantic thermohaline circulation in response to increasing atmospheric CO2 concentration, Geophys. Res. Lett., 32, L12703, doi:10.1029/ 2005GL023209.

Grist, J. P., R. Marsh, and S. A. Josey (2009), On the Relationship between the North Atlantic Meridional Overturning Circulation and the Surface-Forced Overturning Streamfunction, J. Clim., 22, 4989-5002, doi:10.1175/2009JCLI2574.1.

Grist, J. P., and S. A. Josey (2003), Inverse analysis adjustment of the SOC air-sea flux climatology using ocean heat transport constraints, J. Clim., 20, 3274-3295, doi: 10.1175/1520-0442(2003)016%3C3274:IAAOTS%3E2.0.CO;2.

Gulev, S. K., B. Barnier, J.-M. Molines, T. Penduff, and J. Chanut (2007), Impact of spatial resolution of simulated surface water mass transformation in the Atlantic, Ocean Modell., 19, 138-160, doi:10.1016/j.ocemod.2007.07.004.

Häkkinen, S., P. B. Rhines, and D. L. Worthen (2011), Warm and saline events embedded in the meridional circulation of the northern North Atlantic, J. Geophys. Res., 116, C03006, doi: 10.1029/2010JC006275.

Isachsen, P. E., C. Mauritzen, and H. Svendsen (2007), Dense water formation in the Nordic Seas diagnosed from sea surface buoyancy fluxes, Deep-Sea Res. I, 54, 22-41.

Johannessen, O. M., and Coauthors, 2004: Arctic climate change: observed and modelled temperature and sea-ice variability, Tellus, 56A, 328-341

Johnson, G. C., and N. Gruber (2007), Decadal water mass variations along 20W in the northeastern Atlantic Ocean, Prog. Oceanogr., 73, doi:10.1016/j.pocean.2006.03.022.

Josey, S. A., E. C. Kent, and P. K. Taylor (1999), New insights into the ocean heat budget closure problem from analysis of the SOC air-sea flux climatology, J. Clim., 12(9), 2856-2880.

Josey, S. A., J. P. Grist, and R. Marsh (2009), Estimates of meridional overturning circulation variability in the North Atlantic from surface density flux fields, J. Geophys. Res., 114, C09022, doi:10.1029/2008JC005230.

Jungclaus, J. H., H. Haak, M. Latif, and U. Mikolajewicz (2005), Arctic-North Atlantic interactions and multidecadal variability of the meridional overturning circulation, J. Clim., 18(19), 4013-4031.

Jungclaus, J. H., and Coauthors (2006), Ocean circulation and tropical variability in the coupled model ECHAM5/MPI-OM, J. Clim., 19(16), 3952-3972.

Jungclaus, J. H., and Coauthors (2010), Climate and carbon-cycle variability over the last millennium, Climate of the Past, 6, 723-737.

Kalnay, E., and co-authors (1996), The NCEP/NCAR 40-year reanalysis project, Bull. Amer. Meteor. Soc., 77, 437-471.

Krauss, W. (1986), The North Atlantic Current, J. Geophys. Res., 91, 5061-5074.

Langehaug, H. R., I. Medhaug, T. Eldevik, and O. H. Otterå (2011), Arctic/Atlantic exchanges via the Subpolar Gyre, J. Clim., in revision.

Lohmann, K., H. Drange, and M. Bentsen (2009), Response of the North Atlantic subpolar gyre to persistent North Atlantic Oscillation like forcing, Climate Dyn., 32, 273-285, doi: 10.1007/s00382-008-0467-6.

Lumpkin, R., and K. Speer (2003), Large-scale vertical and horizontal circulation in the North Atlantic Ocean, J. Phys. Oceanogr., 33, 1902-1920.

Madec, G., P. Delecluse, M. Imbard, C. Levy (1997), OPA version 8.1 Ocean general circulation model reference manual, 3. LODYC, Technical Report, 91 pp.

Manabe, S., and R. J. Stouffer (1988), Two stable equilibria of a coupled ocean-atmosphere

model, J. Clim., 1(9), 841-866.

Marsh, R. (2000), Recent variability of the North Atlantic thermohaline circulation inferred from surface heat and freshwater fluxes, J. Clim., 13, 3239-3260.

Marsland, S., H. Haak, J. H. Jungclaus, M. Latif and F. Röske (2003), The Max Planck Institute global ocean / sea ice model with orthogonal curvilinear coordinates. Ocean Modelling, 5, 91-127.

Marti, O., and Coauthors (2010), Key features of the IPSL ocean atmosphere model and its sensitivity to atmospheric resolution, Clim. Dyn., 34, 1-26.

Mauritzen, C., S. Häkkinen (1999), On the relationship between dense water formation and the "Meridional Overturning Cell" in the North Atlantic Ocean, Deep-Sea Res. I, 46, 877-894.

McCartney, M. S., and L. D. Talley (1982), The Subpolar Mode Water of the North Atlantic, J. Phys. Oceanogr., 12, 1169-1188.

McDougall, T. J. (1987), Neutral Surfaces, J. Phys. Oceanogr., 17, 1950-1964.

Medhaug, I., T. Furevik (2011), North Atlantic 20th century multidecadal variability in coupled climate models: sea surface temperature and ocean overturning circulation. Ocean Sci., 7, 389-404. doi:10.5194/os-7-398-2011.

Medhaug, I., H. R. Langehaug, T. Eldevik, T. Furevik, and M. Bentsen (2011), Mechanisms for decadal scale variability in a simulated Atlantic meridional overturning circulation, Clim. Dyn., doi:10.1007/s00382-011-1124-z.

Mignot, J., and C. Frankignoul (2010), Local and remote impacts of a tropical Atlantic salinity anomaly, Clim. Dyn., 35 (7-8), 1133-1147.

Munk, W., and C. Wunsch (1998), Abyssal recipes II: Energetics of tidal and wind mixing, Deep-Sea Res., Part I, 45, 1977-2010.

Nurser, A. J. G., R. Marsh, and R. G. Williams (1999), Diagnosing water mass formation from air-sea fluxes and surface mixing. J. Phys. Oceanogr., 29, 1468-1487.

Otterå, O. H., M. Bentsen, I. Bethke, and N. G. Kvamstø (2009), Simulated pre-industrial climate in Bergen Climate Model (version 2): model description and large-scale circulation features, Geosci. Model Dev., 2, 507-549.

Pérez-Brunius, P., T. Rossby, and D. R. Watts (2004), Transformation of the warm waters of the

North Atlantic from a geostrophic streamfunction perspective, J. Phys. Oceanogr., 34, 2238-2256.

Rahmstorf, S. (2002), Ocean circulation and climate during the past 120,000 years, Nature, 419, 207-214.

Rhein, M., and Coauthors (2011), Deep water formation, the subpolar gyre, and the meridional overturning circulation in the subpolar North Atlantic, Deep-Sea Res. II, doi:10.1016/j.dsr2.2010.10.061.

Rhines, P., S. Häkkinen, and S. A. Josey (2008), Is oceanic heat transport significant in the climate system? In Arctic-Subarctic Ocean Fluxes: Defining the role of the Northern Seas in Climate, Dickson, B., Meincke, J., and Rhines, P., editors, 87-109, Springer Verlag.

Roullet, G., and G. Madec (2000), Salt conservation, free surface, and varying levels: a new formulation for ocean general circulation models, J. Geophys. Res. (Oceans), 105(10), 23927-23942.

Servonnat J., P. Yiou, M. Khodri, D. Swingedouw, and S. Denvil (2010), Influence of solar variability, CO2 and orbital forcing during the last millennium in the IPSLCM4 model. Climate of the Past, 6, 445-460.

Smethie W. M., and R. A. Fine (2001), Rates of North Atlantic Deep Water formation calculated from chlorofluorocarbon inventories, Deep-Sea Res. I, 48, 189-215, doi:10.1016/S0967-0637(00)00048-0.

Speer, K., and E. Tziperman (1992), Rates of water mass formation in the North Atlantic Ocean, J. Phys. Oceanogr., 22, 93-104.

Swift, J. H. (1986), The Arctic waters, in The Nordic Seas, edited by B. G. Hurdle, pp. 129-153, Springer-Verlag, New York.

Tandon, A., and L. Zhao (2004), Mixed layer transformation for the North Atlantic for 1990-2000, J. Geophys. Res., 109(C05018), 1-9, doi:10.1029/2003JC002059.

Thierry, V., E. de Boisséson, and H. Mercier (2008), Interannual variability of the Subpolar Mode Water properties over the Reykjanes Ridge during 1990-2006, J. Geophys. Res., 113, C04016, doi:10.1029/2007JC004443.

Trenberth, K. E., and J. M. Caron (2001), Estimates of meridional atmosphere and ocean heat transports, J. Clim., 14, 3433-3443.

Walin, G. (1982), On the relation between sea-surface heat flow and thermal circulation in the ocean, Tellus, 34, 187-195.

Willebrand, J., and Coauthors (2001), Circulation characteristics in three eddy-permitting models of the North Atlantic, Prog. Oceanogr., 48, 123-161.

Zhang, R. (2010), Latitudinal dependence of Atlantic meridional overturning circulation (AMOC) variations, Geophys. Res. Lett., 37, L16703, doi:10.1029/2010GL044474.